u Ottawa

L'Universite canadienne
Canada's university

FACULTE DES ETUDES SUPERIEURES
ET POSTOCTORALES

u Ottawa
L'Universite canadienne
Canada's university

FACULTY OF GRADUATE AND
POSDOCTORAL STUDIES

Gregoire Berube
AUTEUFDEIATHESETAUTHOR

M.A.Sc. (Mechanical Engineering)

School of Information Technology and Engineering
'TACULTTEC^

Development of Metastable Aluminum Alloy Coatings and Parts for Automotive Applications

TITRE DE LA THESE / TITLE OF THESIS

Bertrand Jodin
DIRECTEUR'PRECTR

CO-DIRECTEUR (CO-DIRECTRICE) DE LA THESE / THESIS CO-SUPERVISOR

EXAMINATEURS (EXAMINATRICES) DE LA THESE/THESIS EXAMINERS

X. Huang

M. Nganbe

Gary W. Slater
Le Doyen de la Faculte des etudes superieures et postdoctorales / Dean of the Faculty of Graduate and Postdoctoral Studies

DEVELOPMENT OF METASTABLE ALUMINUM ALLOY COATINGS AND PARTS FOR AUTOMOTIVE APPLICATIONS

Gregoire Berube

A thesis submitted to the Faculty of Graduate and Postdoctoral Studies

in partial fulfillment of the requirements for the degree of

MASTERS OF APPLIED SCIENCE

in Mechanical Engineering

Ottawa-Carleton Institute for Mechanical and Aerospace Engineering

University of Ottawa, Ottawa, Canada

October 2009

Abstract

In this study, a metastable Al-Fe-V-Si alloy powder was produced by rapid solidification using the gas atomization process. The alloy composition was chosen for its mechanical properties at elevated temperature for potential applications in internal combustion gasoline engines. The microstructural properties of the Al-Fe-V-Si powder were determined through transmission electron microscopy imaging and selected area electron diffraction indexing, energy dispersive spectroscopy, X-ray diffraction and differential scanning calorimetry. Three distinct microstructures were observed as well as two different phases, namely a Ali3(Fe,V)3Si silicide phase and a metastable $(Al,Si)_x(Fe,V)$ micro-quasicrystalline icosahedral (MI) phase. The metastable MI phase was determined to be thermally stable up to 380°C, after which a phase transformation to silicide occurs. The Cold Gas Dynamic Spraying (CGDS) process was used to produce coatings of the alloy. This spray process was selected due to its relatively low operating temperature, thus preventing significant heating of the particles during spraying and as such allowing the original microstructure of the feedstock powder to be preserved within the coatings. Coatings were produced by CGDS using Helium and Nitrogen as propellant gases. The coatings microstructure was investigated using scanning electron microscopy and transmission electron microscopy analyses. The mechanical properties of the coatings were then evaluated through bond strength testing and microhardness testing.

Resume

Un alliage metastable d'Al-Fe-V-Si en poudre a ete produit par solidification rapide en utilisant le procede d'atomisation par gaz. La composition chimique a ete choisie pour les proprietes mecaniques qu'elle procure a temperatures elevees, permettant ainsi l'utilisation de l'alliage dans les moteurs a essence a combustion interne. Les proprietes de la microstructure de l'alliage ont ete determinees a l'aide de microscopie a transmission electronique, de l'indexation de la diffraction electronique d'aire selectionnee, la spectroscopic a dispersion d'energie, la diffraction des rayons X, et la calorimetrie a balayage differentiel. Trois microstructures distinctes ont ete observees de meme que deux phases differentes, soit une phase de siliciure Ali3(Fe,V)3Si ainsi qu'une phase micro-quasicrystalline icosahedrale (MI) sous la forme (Al,Si)*(Fe,V). La phase MI metastable fut determinee comme etant thermiquement stable jusqu'a 380°C, apres quoi la phase se transforme en siliciure. Le procede de deposition dynamique a gaz froid a ete utilise par la suite afin de produire des revetements a partir de l'alliage. Ce procede fut selectionne pour sa temperature d'operation relativement basse, prevenant ainsi une augmentation de la temperature des particules lors de la deposition, ce qui permet de preserver la microstructure originale de la poudre dans le revetement. De l'helium et de l'azote ont ete utilises pour produire des revetements par la deposition a froid. La microstructure des revetements fut investiguee par analyses de microscopie a balayage electronique et a transmission electronique. Des essais de force d'adhesion et de microdurete ont servi a determiner les proprietes mecaniques des revetements.

Acknowledgements

The author would first like to thank Bertrand Jodoin for suggesting the idea behind this project as well as providing guidance and advice throughout the research. The author would also like to acknowledge the help and support from the staff of the University of Ottawa - Mechanical Engineering machine shop. In addition, the experimental results of this research were obtained with the help of the following students: Patrick Richer, Eric Sansoucy, Karen Taylor, Eric Matte and Mohammed Yandouzi.

Special thanks are given to Leonardo Ajdelsztajn and his team for atomizing the Al-alloy powder that was used for this research. The author is also very grateful for all the help and mentorship on transmission electron microscopy done at the University of Chile under the supervision of Alejandro Zuniga.

The author would like to acknowledge the financial support of the following organizations, which made this research possible: Ontario Graduate Scholarship, Fonds Quebecois de Recherche sur la Nature et les Technologies, Centerline (Windsor) Limited, Materials and Manufacturing Ontario, and Ontario Centres of Excellence.

Finally, the author would like to thank his family and friends for their support and would like to dedicate his thesis to Koto and Jocelyne.

Table of Contents

List of Figures

List of Tables

Glossary

Critical Velocity: Velocity above which the particles must travel in order to gain enough kinetic energy to plastically deform upon impact with the substrate.

Differential Scanning Calorimetry (DSC): An analytical technique in which the difference in the amount of heat required to increase the temperature of a sample and reference are measured as a function of temperature.

Dispersoids: Finely divided particles of a substance dispersed in another.

Energy Dispersive Spectroscopy (EDS): Investigation of a sample through analyzing X-rays emitted by the matter in response to being hit with charged particles. Each element has a unique atomic structure allowing x-rays to be identified uniquely from each other.

Equiaxed: Crystals exhibiting similar dimensions in all directions.

Grain: An individual crystal in a metal.

Greenhouse Gases (GHG): Gases in the atmosphere that absorb and emit radiation within the thermal infrared range.

Icosahedral: A polyhedron having 20 faces.

Intermetallic: A material composed of two or more metals or of a metal and a nonmetal.

Metastable: A state which has greater energy than another stable state, yet incapable of spontaneous change to the other. It is marked by a slight margin of stability.

Microhardness: Hardness measured under light loads, from 5 to 2 000 grams, to involve only specific elements of the materials investigated.

Microstructure: The microscopic structure of a material, its arrangement of atoms.

Nitrous Oxides (NO_x): A generic term for mono-nitrogen oxides (NO and NO2). These oxides are produced during combustion, especially combustion at high temperatures.

Phase: A single solid state of a material.

Porosity: The degree to which a coating contains pores.

Precipitate: A substance separated from a solution or suspension by chemical or physical change usually as an insoluble amorphous or crystalline solid.

Quasicrystalline (QC): A state of solid material that resembles a crystal in being composed of repeating structural units but that incorporates two or more unit cells into a quasiperiodic structure.

Scanning Electron Microscope (SEM): An electron microscope in which a beam of focused electrons moves across the object, where electrons are collected to form a image.

Selected Area Electron Diffraction (SAED): A technique used in transmission electron microscopy (TEM) where a parallel beam of electrons is diffracted as it passes through the sample. Each diffraction spot corresponds to a satisfied diffraction condition of the sample's crystal structure.

Shear Adiabatic Instability: When a material experiences plastic deformation at high levels, releasing strain energy in the form of heat and increasing the temperature of the material.

Shockwave: A fully developed compression wave of large amplitude, across which density, pressure, and particle velocity change drastically.

Thermal Barrier Coating (TBC): Coatings which insulate metallic components from large and prolonged heat loads by utilizing thermally insulating materials.

Transmission Electron Microscopy (TEM): A microscopy technique utilizing a beam of electrons that is transmitted through a specimen, where the electrons interact with the atoms as they pass trough the specimen.

X-Ray Diffraction (XRD): An investigation technique which relies on the pattern formed by the diffraction of a parallel beam of X-rays falling upon a substance with planes of regularity in its structure.

1 Introduction

The following pages begin with an introduction of the current fuel consumption trends in the transportation sector, more specifically the automobile industry, and the motives that prompted this research project. A brief description of recent developments in material engineering follows, namely advancements in the development of high-temperature aluminum alloys that allow the possibility of increasing fuel efficiency in gasoline engines. Finally, conventional fabrication methods and coating technologies are presented along with their limitations with respect to aluminum alloys. The specific research objectives are stated at the end of this chapter.

1.1 Current Fuel Trends

Interest and demand for motor vehicles with increased fuel economy is attributed to current hikes in fuel price as well as environmental concerns. Actual fuel price at the pump may cause individuals to reconsider replacing their vehicle by a more economical model. During the last fuel price crisis in the United States of America (USA), the Corporate Average Fuel Economy (CAFE) enactment was introduced (in 1975) to compel car manufacturers to develop more fuel-efficient vehicles. In most cases, prices were actually lowered on fuel-efficient models to boost sales in order for the manufacturers to attain the CAFE standard. If the standard was not met, a penalty was paid for each vehicle sold that didn't maintain the set standard. However, most improvements in car engine fuel economy were achieved between 1975-1980 and have stagnated ever since. Consumers kept buying more and more luxury vehicles, which are

inherently less fuel-efficient, thus explaining the stagnation in the CAFE [1], In the year 2004, the average fuel economy of all cars on the road was 11.8 litres /100 km, while the average for new cars was 9.8 litres /100 km [2].

Environmental issues related to fuel economy are of equal concern to many consumers and perhaps involve more of a global responsibility. Consensus among the scientific community agrees that we need to reduce greenhouse gases (GHG) by more than 50% by the year 2050 in order to have high confidence of avoiding disastrous impact on the earth's climate [3]. Transportation is the source of about one third of the USA carbon dioxide emissions today and is projected to generate about one third of the 40% rise in the USA carbon dioxide emissions forecast for 2030 [4]. In the absence of strong government policies, it is projected that the worldwide use of oil in public transport will nearly double between 2000 and 2030, leading to a similar increase in GHG emissions [5],

One plausible strategy to achieve significant reductions in projected vehicle petroleum use and CO2 emissions by 2025 is fuel efficiency. The best strategy for achieving the 2050 targets is a plug-in hybrid running on a combination of low-carbon electricity and a low-carbon fuel, probably biomass derived [3]. Ideally, these advanced hybrids would also be a flexible fuel vehicle capable of running on a blend of biofuels and gasoline. Such a car could travel over 200 kilometers on one litre of gasoline (and 19 litres of cellulosic ethanol) and have less than one-tenth the GHG emissions of current hybrids [6].

Much has also been said about hydrogen-powered vehicles, either through direct combustion or driven by fuel-cell technology. Hydrogen is the most abundant element on earth and promises only pure water vapour as emission from its combustion. However, substantial investments are required to develop the technology, the infrastructure and distribution network to support it. Instead of hydrogen cars, a much better option remains the hybrid gasoline-electric vehicle, because it can reduce the gasoline consumption and GHG emission by 30% to 50% with no change in vehicle class, and hence no loss of jobs and no compromise on safety or performance. Because of these advantages, it, and not hydrogen-powered automobiles, will likely become the dominant vehicle platform by the year 2020 [6],

1.2 Fuel Efficiency and Fuel Economy

Recent research in the area of fuel economy can generally be divided in three main categories: weight reduction, reduced friction and increased engine operating temperature. The latter directly affects the internal-combustion (IC) engine efficiency and performance improvements have been observed when increasing the engine operating temperature (EOT) [7]. The Otto cycle, or the constant volume heat addition model, under a few basic assumptions, can represent a spark-ignited gasoline engine. The first assumption is that the combustion is assumed to be rapid enough that the piston does not move during the combustion process, thus combustion occurs at constant volume. The working fluid in the Otto cycle is also assumed to be an ideal gas and that it has a constant specific heat value. These assumptions are used to simplify the mathematics to

produce the schematic representation of the Otto cycle shown in figure 1.1. The four basic processes of the Otto cycle are: isentropic compression (1-2), constant-volume heat addition (2-3), isentropic expansion (3-4) and constant-volume heat rejection (4-1). From figure 1.1, it can be observed that by increasing the temperature of combustion (2-3), the internal energy is also increased. Therefore, if the combustion temperature can be increased for a given fuel input, the power output will also increase resulting in a better fuel efficiency. Similarly, by increasing the combustion temperature, it is possible to reduce the fuel input and maintain the same power output, which also translates in better fuel efficiency.

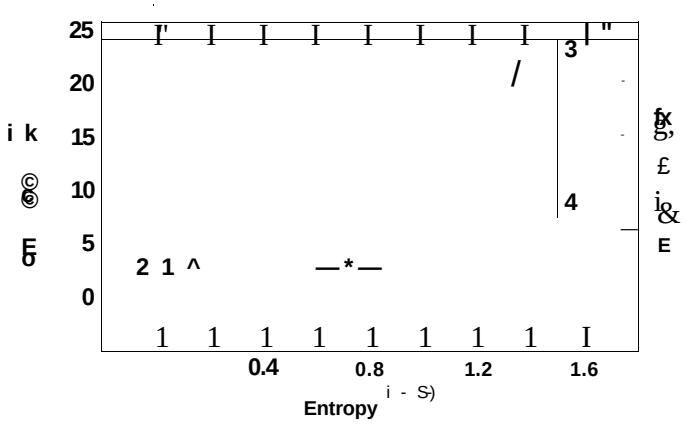

Figure 1.1: Graphical representation of the Otto cycle [8].

Various studies have already demonstrated the benefits of increasing the engine operating temperature. One study done by Buyukkaya *et al.* on an engine whose pistons were coated with MgZrOs over a NiCrAl bond coat demonstrated that reductions between 1% to 8% in fuel consumption could be achieved by the effect of the thermal barrier coating (TBC) [9]. Similarly, another study done on an engine with its combustion chamber and

pistons coated with CaZrCb and MgZrC>3 ceramics over a NiCrAl bond coat demonstrated improvements of up to 5% in effective efficiency over various loading conditions [10].

The purpose of this present study is also to enable the increase in the engine operating temperature (EOT) in order to achieve similar improvements in efficiency. However, it is proposed to use another approach than TBC technology to achieve this goal. TBCs require specific substrate surface preparation and also need a bond-coat layer between the substrate and ceramic coating, which acts as a buffer between the differences in thermal expansion coefficients of the substrate and ceramic. The brittle behaviour of ceramics can also lead to breakage and failure during operation. Instead, another approach is proposed, which is less complicated and less costly than TBCs. The new approach shall increase the EOT by controlling and limiting the heat losses in the combustion chamber through the engine's cooling system, rather than limiting heat losses with a TBC. By reducing the load on the cooling system, less energy is transfer to it and more heat is retained within the combustion chamber, resulting in the retention of a more elevated EOT.

1.2.1 Effect of Increased EOT on NO_x Emissions

During the combustion process, nitrogen oxides (NO_x) are formed within the combustion chamber from the reaction between nitrogen and oxygen atoms present in the air. The reactions forming NO_x are very temperature dependent, so the NO_x emissions from an engine scale proportionally to the engine load [8]. In spark ignition engines, the dominant component of NO_x is nitric oxide NO, which is formed in the high temperature burned gases left behind by the flame front. Therefore, if the EOT is increased to improve the

effective efficiency without making other modifications, it can be expected that NO_x emissions will also increase. However, simple adjustments and modifications can be done to bring the NO_x emissions to levels similar to those present prior to the increase in EOT. For example, dilution of the intake charge by residual gas, explicitly via exhaust gas recirculation, implicitly via throttling, or by moisture in the inlet air, can all reduce the nitric oxides [8].

1.3 Engine Parts, Materials and Alloy Properties

Aluminum alloys are the current material of choice for IC engine parts mostly due to their reduced weight, however they exhibit a sharp decrease in mechanical properties when exposed to temperatures above 300°C [11]. The maximum temperature seen on the top face of a conventional Al-alloy piston is on the order of 285 °C, according to a study using numerical modeling with commercial code (ANSYS)[12]. The surface temperature increases to 366 C, 28% higher than the uncoated piston, after applying a TBC consisting of MgZr03 and NiCrAl as the bond coat [12]. The TBC effectively reduces heat losses in the combustion chamber by limiting thermal conduction through the top face of the piston. In this work, the goal is to be able to reach a similar increase in temperature in order to gain similar efficiency improvement as indicated previously, but without the use of a TBC. However, current conventional aluminum alloy systems are incapable of sustaining such an increase in temperature without suffering a decrease in mechanical properties, resulting in engine failure.

Advances in aluminum-based alloy development are maintaining it as the material of choice for IC engine pistons. In the past decade, increased efforts have been made to improve the high temperature properties of such alloys. These alloys are usually pressed or cast into the desired piston shape or thermally sprayed as coatings. More recently, rapid solidification (RS) processing combined with consolidation techniques has been used to produce pistons [11]. RS improves the alloy's mechanical properties in terms of increased tensile strength and ductility as well as fatigue and crack propagation resistance [11]. Such improvements are associated with large solid solubility extensions of alloying elements, reduced macro-segregation, refinement of the alloy grain size and changes in the second phase particle size, shape and distribution [13]. However, coarsening of the microstructure is always found due to the high temperatures involved during consolidation [11]. Consequently, the alloy properties, such as strength at moderately high temperatures of an IC engine, are reduced and the great potential of RS is far from being fully exploited [11].

In order to increase or maintain the mechanical properties of aluminum alloys at higher service temperatures, it is proposed to select an alloying system that will allow the stabilization of the structure at high temperatures. This can be achieved by changing and complicating the phase composition through the addition of transition metals that are highly soluble in the liquid A1 but insoluble in the solid state, which enter in solid solution during solidification and inhibit diffusion in aluminum. The basic requirement for forming thermally stable dispersoids in the microstructure is that the alloying elements should have low solid solubility and low diffusivity in A1 to have a minimal

coarsening during high temperature exposure. Additionally, some interfacial coherency is desired in order to minimize dispersoid growth at elevated temperatures. The microstructure resulting from the RS process usually consists of very fine intermetallics (dispersoids) in an aluminum matrix. The intermetallic phases in the aluminum matrix are the main features responsible for the increased mechanical strength at room and high temperatures [11]. However, the intermetallic phase is brittle in nature and if agglomeration and coarsening occurs, the alloy loses its desired mechanical properties. As such, alloys should be solidified very rapidly to form the required intermetallic phase or their precursors on a fine scale and not to form coarse intermetallics. The elevated temperatures involved in casting and powder metallurgy induce this coarsening and as such, large parts have not been successfully produced via these routes.

1.3.1 Metastable Al-Fe-V-Si Alloy

The discovery of icosahedral and other quasicrystalline phases in the Al-Mn binary system has prompted research on these phases in a multitude of Al-based alloy systems. Results of an investigation on the binary Al-Fe system have reported that in this system, an icosahedral phase can be produced over a wide range of iron content and that the thermal stability boundary for this phase rises very sharply [14]. The addition of ternary or quaternary elements provides additional binary dispersoids, which stabilize the existing Al-Fe binary intermetallics or form ternary or quaternary intermetallics having a more symmetrical lattice structure. Vanadium additions to the Al-Fe binary alloys affect the thermal stability to a much greater extent than do iron additions to Al-V binary alloys, implying that maximum thermal stability in the ternary alloy is attained in chemistries

that favor iron over vanadium [15]. Furthermore, the addition of the quaternary element vanadium substitutes iron in the Al-Fe-Si intermetallic, which stabilizes its structure. It is proposed in this work to use an Al-Fe-V-Si alloy, as it has demonstrated to have the best combination of room-temperature and elevated-temperature mechanical properties, which make these alloys suitable for applications at elevated temperatures up to 350 °C [16]. Such an alloy can be used to apply a protective layer on top of internal engine parts that will resist the increased temperature and also protect the underlying substrate, or can be used to replace the part altogether.

1.4 Al-Fe-V-Si Alloy Production Methods

Most alloys prepared using RS methods are found in powder form since the small spherical particle offers the highest surface are to volume ratio (i.e. 3/d), thus enabling very high cooling rates through convective heat transfer over a high surface area for a relatively small volume or mass. Conventional methods for producing metal alloy powder consist of melt atomization techniques, which can be divided in four categories: air atomization, inert gas atomization, water atomization, and centrifugal atomization. It is estimated that 1 200 000 tons of metal powder are produced annually, of which 100 000 to 150 000 tons are aluminum and aluminum alloys [17]. Almost all of the aluminum powders (99% of total production) are produced by air atomization, while the remainder is produced by inert gas atomization [17].

The atomization processes differ only in the medium used for atomization, with the exception of centrifugal atomization. In centrifugal atomization, or melt spinning, a liquid

stream of molten metal drops onto a spinning disk rotating at high velocities and when the stream hit the rotating disk, it is broken into small droplets which are thrown outwards at high velocities. The droplets then solidify very rapidly before hitting the chamber walls of the atomizer. However, the melt spinning technique can sometimes produce ribbon shapes rather than fine powder particles, due to long duration of time the molten metal is exposed to the atmosphere before being solidified. The melted metal can be provided by conventional melting methods, such as an induction or arc furnace, or by melting a continuously fed alloy wire using an electrical arc.

In the other atomization process, the molten metal is placed in a tundish, which is a reservoir terminated by an orifice that feeds a constant stream of metal into the atomizing chamber. The liquid metal is then broken into fine droplets as the result of a high velocity jet of the atomizing medium (air, gas or water) impacting the stream of molten metal. Metal droplets then solidify before being collected at the bottom of the atomizing chamber. Schematic representations of the centrifugal, water and gas atomization are illustrated in figure 1.2.

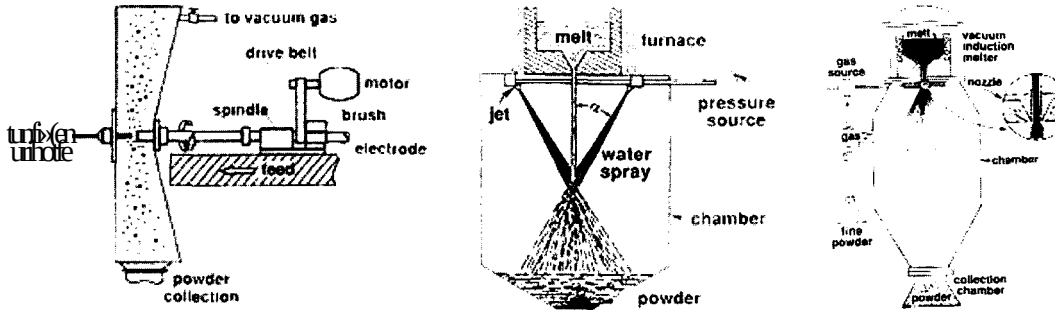

(a) (b) **(c)**

Figure 1.2: Schematic representation of (a) centrifugal atomization, (b) water and (c) gas atomization processes. Source "Powder Metallurgy Science" Second Edition, R.M. German, MPIF.

The atomization medium (fluid) has a great impact on the cooling rates of solidification of the liquid metal droplets during atomization. The variations are mainly due to the differences in thermodynamic properties of the atomizing medium, more specifically the specific heat capacity (c_p). Atomizing mediums that possess higher specific heat capacities will result in higher cooling rates. Accordingly, the highest cooling rates are found using helium (c_p = 5.193 kJ/kg-K), followed by water (c_p = 4.217 kJ/kg-K), nitrogen (c_p = 1.041 kJ/kg-K) and air (c_p = 1.007 kJ/kg-K). Air is the most practical and economical to use, however the effect of oxidation of the metal powder particles cannot be neglected. As such, an inert gas, such as nitrogen, may be a suitable replacement. For this study, very high cooling rates are sought in order to ensure the formation of the metastable phases in the Al-alloy. Helium will provide an inert and non-reactive atmosphere and elevated cooling rates. Although a more economical option, water must be rejected as molten aluminum and water can create violent explosion when mixed.

1.5 Thermal Spray Overview

As denoted previously, conventional consolidation methods are unable of producing large metallic parts made of metastable Al-alloy due to the temperature sensitive nature of the intermetallic phase, which is inherently responsible for the high mechanical properties of the alloy. However in most cases, the required properties are often only needed on the outer surface of the part, showing the need for coating and surface technologies. In many applications, a part is subjected to multiple stresses under harsh environments and often one single material or alloy cannot accomplish by itself. Instead, a material possessing the combined properties of several materials at once would be required. Unfortunately, such materials, with multiple combined properties, have yet to be discovered. However, by applying a surface enhancement, such as a thermally sprayed coating, it is possible to have the best properties of multiple materials in one single part. The underlying concept behind coating technologies is that the base material, or substrate, is first selected as the material which is best suited for its application (eg. for its strength, toughness, etc.). A surface enhancement is then applied as a thin layer made of a material that is chosen for its specific properties to fulfill the deficiencies in the properties of the base material. Depending on the coating technology, coating thicknesses can vary from less than 1 micrometer to a few hundred micrometers. The major areas in which coating technologies are used include wear resistance, corrosion resistance and thermal protection.

In this study, it is proposed that conventional aluminum alloys continue to be used for pistons in IC engines, but a thin coating of metastable Al-Fe-V-Si alloy be applied on the piston crown using a coating technology. Eventually, the entire piston could be fabricated from the metastable Al-alloy but this is not the scope of the current work. A brief review of current thermal spray technologies is presented below, followed by a more in-depth description of the Cold Gas Dynamic Spray (CGDS) process in the second chapter, which is believed to be a coating technology than can preserve the metastable phase of the Al-Fe-V-Si alloy.

1.5.1 Plasma Spray

In plasma spray, powder particles are accelerated and melted (or partially melted, depending on the material) as they are injected in a jet of ionized gas called plasma. In most cases, the plasma jet is formed when a gas flow is rapidly heated as is passes through an electrical arc created between an anode and cathode. The anode and cathode are configured in a concentric fashion inside the plasma torch as shown in figure 1.3. The gas used in plasma spray is generally a mixture of Ar-H2-He due to increased thermal conductivity of the plasma gas [18]. Plasma torches can produce plasma jets with high temperatures (10,000 to 14,000 K in the jet core) resulting in fully molten particles upon impact with velocities below 300 m/s [18]. However, the process is not very well suited for materials that are sensitive to oxidation. To reduce particle oxidation, higher particle velocities with lower temperatures have to be achieved [18]. In order to overcome oxidation, variations of the atmospheric plasma spray technique have been developed, such as vacuum plasma spray (VPS) and low-pressure plasma spray (LPPS), to reduce or

eliminate oxygen content in during the spraying process. One of the benefits of the plasma spray process is that it remains one of the only commercial processes capable of producing coating made of ceramic materials, due to the elevated temperature of the process. The drawback of this method is its elevated temperature, making this process unsuitable for temperature sensitive materials, such as the Al-Fe-V-Si alloy used in this study.

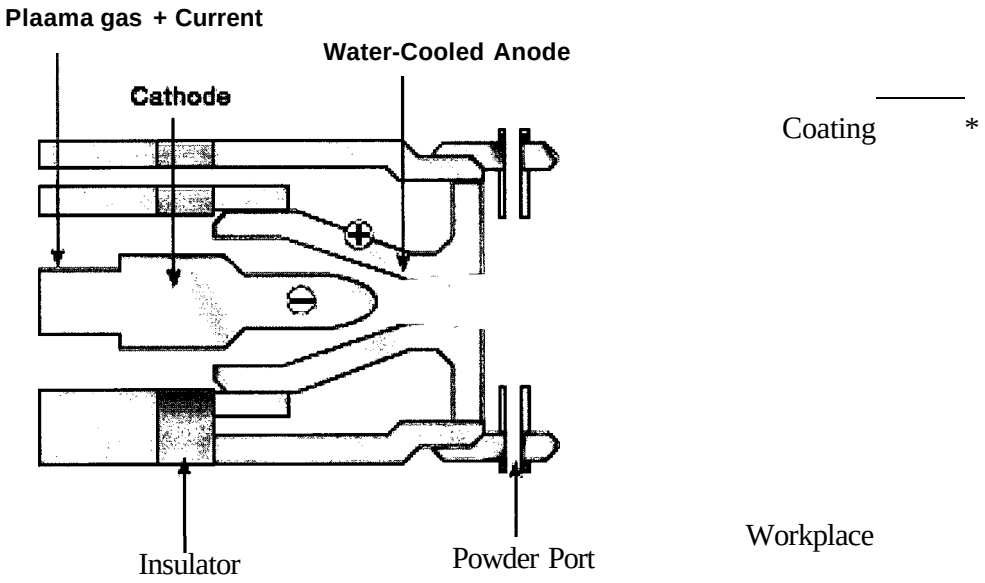

Figure 1.3: Schematic representation of the Atmospheric Plasma Spray (APS) process.

Source "www.SulzerMetco.com".

1.5.2 High Velocity Oxygen Fuel (HVOF) Spray

The HVOF process is similar in nature to the plasma spray process in that powder particles are heated and accelerated in a jet of heated gas and projected on the substrate surface. The difference between HVOF and plasma spray is that the heated jet of gas in

HVOF is produced by the combustion of a high-pressure fuel/ oxygen mixture. Gas fuels typically used are propane, propylene, methane and hydrogen, while kerosene is used as a liquid fuel. Most HVOF torches operate at pressures up to 1.35 MPa, however newer torch design using oxygen and kerosene can work with pressures up to 4.2 MPa, where particle velocities can reach 1000 m/s [18]. A schematic representation of the HVOF process is illustrated in figure 1.4.

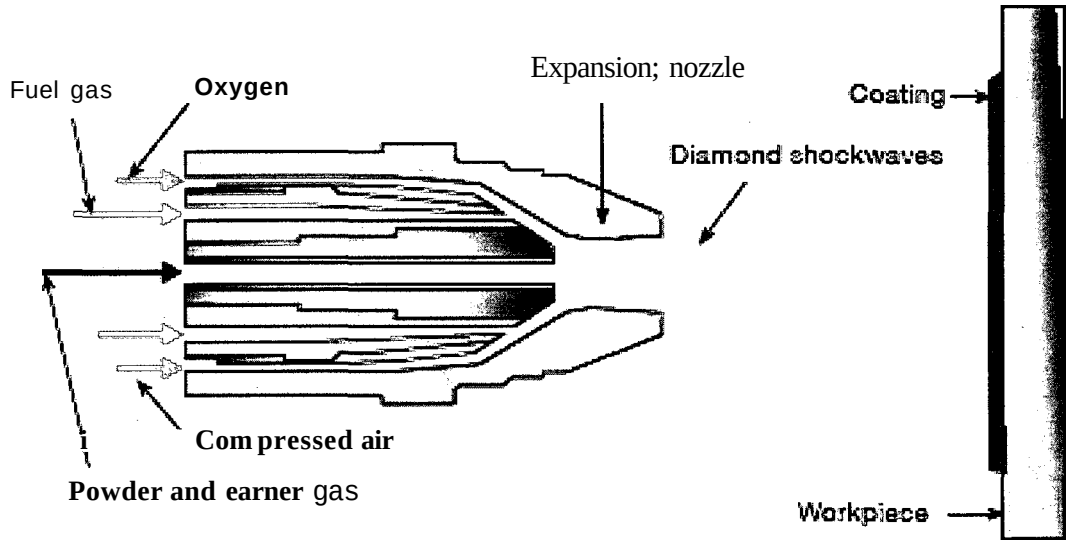

Figure 1.4: Schematic representation of the High Velocity Oxigen Fuel (HVOF) process.

Source "www.SulzerMetco.com".

Although the powder particles are traveling at higher velocities, thus exposed a shorter amount of time to the hot gases and also at a lower temperature compared to plasma spray, the process temperature is still sufficiently high to threaten the metastable phases of the Al-alloy which is the scope of this thesis.

1.5.3 Other Thermal Spray Processes

The D-Gun™ (Detonation Gun) process is another coating process used to produce high quality coatings. Again, a high velocity jet of hot gases is used to project the powder particles onto the substrate surface to form the coating. Here, the hot gases are produced by the detonation of an oxygen-fuel mixture, where a metered amount of oxygen and fuel, usually acetylene, are injected along with the powder particles at the closed end of a long barrel, and a spark ignites the mixture. The high pressure, high temperature gases that follow the Shockwave produced by the detonation accelerate the powder particles towards the substrate. A pulse of nitrogen gas is used to purge the barrel between each detonation and the process is repeated several times a second. Figure 1.5 illustrates a schematic representation of the D-Gun™ process. Every pulse deposits a small disk shaped layer of coating a few micrometers thick and many overlapping "disks" produce the final coating. The D-Gun™ process is known for producing dense coatings and is also used to form coatings made of very hard materials such as cobalt tungsten carbide (WC-Co) [18]. However, as the powder are exposed to high temperatures during the process it must also be rejected for the current work since it could once again endanger the delicate phases in the Al-Fe-V-Si, drastically reducing its mechanical properties.

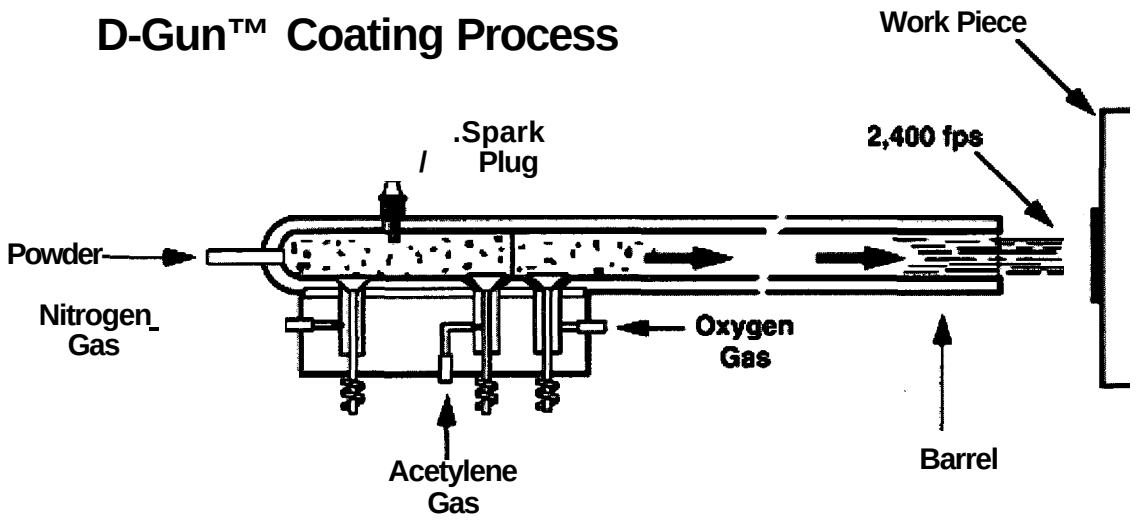

Figure 1.5: Schematic representation of the D-Gun™ process. Source "www.Praxair.com".

A new process developed at the University of Ottawa, called Pulsed Gas Dynamic Spraying (PGDS), has the potential to overcome this problem as it doesn't involve any combustion or detonation, which may affect the microstructure of the Al-alloy powder. The process has some similarities with the D-Gun™ process as the powder particles are accelerated in the high-pressure gas flow left behind a Shockwave. In the PGDS process, a high-pressure inert gas, helium or nitrogen, is trapped behind an actuator in the closed end of a long barrel-shaped nozzle. Once the actuator is opened, the successive expansion waves of the high-pressure gas coalesce in the quiescent gas ahead of the actuator to form a Shockwave. Powder particles are injected right before the actuator is opened. The actuator is closed, the system pressurized again, and the process is repeated several times per second. The experimental set-up of the PGDS process developed at the University of

Ottawa is schematically illustrated in figure 1.6. The process has successfully produced coatings made of copper, zinc, 5083 aluminum alloy, Al-12Si alloy and nanocrystalline WC-15CO [19].

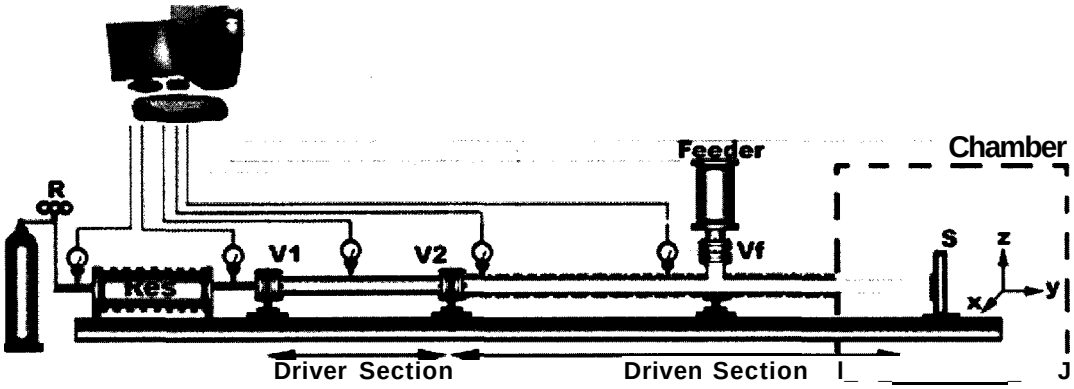

Figure 1.6: Schematic representation of the Pulsed-Gas Dynamic Spraying (PGDS) experimental set-up developed at the University of Ottawa.

The feasibility of using this new process was not evaluated in this study as it was still in its development phase when this study was underway. However, the PGDS process has promising potential to apply coatings of metastable Al-Fe-V-Si alloy on piston crowns and should be compared to the Cold Gas Dynamic Spray (CGDS) process in a future study. Here, the CGDS process was the chosen technology to apply the Al-alloy coating. The underlying theory behind the CGDS process is described in the following chapter.

1.6 Research Objectives

The objectives of the thesis are two-fold: develop a metastable aluminum alloy using rapid solidification techniques and produce functional coatings from the alloy powder. Once the alloy powder is produced, its phases are to be identified and thermal stability determined. Then, coatings will be produced using the CGDS process and evaluated to ensure phases preservation and thermal stability is unaffected by the coating process. Using nitrogen as the process gas, to demonstrate a more economical possibility for the industry, will also be investigated.

2 The Cold Gas Dynamic Spraying Process

The Cold Gas Dynamic Spraying process was chosen to produce metastable Al-Fe-V-Si coatings as it can rapidly produce an appreciable thickness of material, while preserving the original feedstock microstructure and chemical composition. It is envisioned that near net shapes could be fabricated using the CGDS process, thus creating large metastable alloy parts which was not previously possible using conventional consolidation techniques. The CGDS process development and theory is presented in the next paragraphs, followed by the process advantages.

Based on previous studies reporting successful coating production of temperature sensitive materials such as nanocrystalline materials [20], it is envisioned that the CGDS process represents a promising solution to the production of metastable alloy coatings. The CGDS process uses a supersonic gas flow to accelerate fine solid particles beyond a critical velocity above which the particle will plastically deform and adhere to the substrate surface upon impact. Various materials have already been successfully deposited onto diverse substrates using the CGDS process [20-24]. As opposed to other conventional spraying processes, the CGDS process does not involve any melting of the particles to produce coatings. Rather, the particles remain near room temperature during the process, thereby minimizing oxidation and avoiding grain growth within the coating [24]. As such, the CGDS process is often referred to as a solid-state process. This represents a major advantage over other consolidation techniques since the original microstructure and chemical composition of the powder is preserved.

2.1 Cold Gas Dynamic Spray Theory

Alkimov, Papyrin and their team discovered the CGDS process during supersonic wind tunnel testing at the Institute of Theoretical and Applied Mechanics of the Siberian Division of the Russian Academy of Science in Novosibirsk [25]. They noticed that small metallic tracer particles introduced in the supersonic flow during testing began adhering and building on the surface of the model above a certain particle velocity. Below this velocity, the particles simply eroded the model's surface [26]. The Russian discovery was developed in a coating technology, after successfully forming numerous coatings made of pure metals, alloys, composites and also polymers [27]. In 1994, Alkhimov, Papyrin *et al.* obtained a U.S. Patent for the CGDS process [28].

The CGDS setup consists of a converging-diverging (or De Laval) nozzle connected to a high-pressure gas supply, called propellant gas, and a separate gas supply, named carrying gas, which transports the powder particles. The propellant gas is also sometimes heated in a gas heater to increase its temperature before entering the nozzle. A typical CGDS setup is schematically illustrated in figure 2.1.

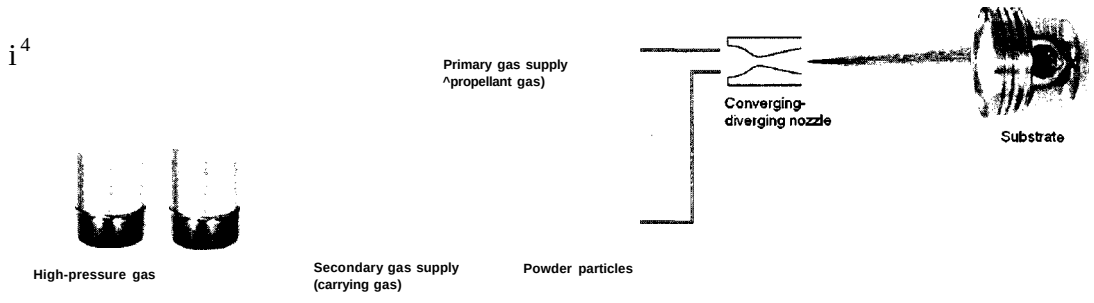

Figure 2.1: Schematic representation of the CGDS process setup.

The high-pressure gas is accelerated to supersonic velocities in the convergent-divergent nozzle, due the specific nozzle geometry. The gas accelerates from a subsonic velocity to sonic velocity in the convergent section of the nozzle. In order to obey mass conservation, the velocity must accelerate to compensate for the reduction in flow area in the convergent section (in the subsonic regime). Once the flow reaches sonic velocity, or Mach 1 at the junction of the convergent the divergent section, which is called the throat, the flow needs to expand in a divergent section in order to continue to increase its velocity above Mach 1. To maintain the conservation of mass, due to an increase the cross-sectional area, the gas density must decrease in order to compensate (in the supersonic regime). As a result of the expansion in the divergent section, the gas temperature decreases along with the density as the velocity increases. Furthermore, the nozzle geometry directly impacts the gas exit velocity as the ratio between the nozzle exit area and throat area dictates the nozzle Mach number [29]. A previous study has demonstrated that the optimal nozzle Mach number for CGDS should be between 1.5 and 3 [24],

The gas exit velocity is obtained by multiplying the nozzle exit Mach number and the sonic velocity of the working gas. In turn, the gas sonic velocity is dependant on gas properties, namely its molecular weight (M), heat capacity ratio (y) and temperature (T) according to equation (2.1):

$$\upsilon_{sonic} = \sqrt{\frac{\gamma RT}{M}} \qquad ...(2.1)$$

From this equation, there are two ways to maximize the exit gas velocity: selecting gases with low molecular weight and increasing the gas temperature. Helium is often selected for CGDS due to its low molecular weight (M=4.0026). Nitrogen is a more economical option, however its molecular weight is 7 times higher (diatomic nitrogen, M=28.0134). Secondly, the propellant gas can also be heated to increase the velocity. Equation 2.1 shows that an increase in gas velocity is proportional to the square root of the increase in gas temperature. Even if the gas is heated, the powder particles remain well below their melting temperatures as the temperature of the propellant gas rapidly decreases as the gas expands in the divergent section [27].

Another important parameter in CGDS is the stagnation pressure, **Po.** If the stagnation pressure is too low, the flow will become over expanded and a Shockwave will form in the divergent section, inside the nozzle as to increase the pressure to match atmospheric pressure. On the other hand, if the stagnation pressure is too high, the flow will be under expanded and the Shockwave will be outside the nozzle to accommodate the pressure in the gas jet to atmospheric pressure. It is always better to have the Shockwave outside the nozzle, as close as possible to the substrate, since a Shockwave can potentially slow down the powder particles. If the particles are slowed down significantly, the coating will not be formed. Figure 2.2 illustrates the evolution of pressure inside a convergent-divergent nozzle. For a given inlet pressure **(Po),** velocity will increase in the subsonic regime (M<1) up until the throat. Velocity will be exactly sonic at the throat (M=l) when critical pressure is reached at the throat. If the outlet pressure is too low with respect to the inlet

pressure, the flow simply decelerates to subsonic velocity (M<1) after passing the throat, undergoing a subsonic diffusion. When the inlet pressure is increased, the velocity will continue to increase to a supersonic regime (M>1) after the throat, however, if the outlet pressure is still too low compared to the inlet pressure, a normal shock develops inside the nozzle in the diverging section. The shock instantly increases the pressure and the velocity drops to a subsonic regime (M<1). Increasing the inlet pressure further pushes the normal shock outside until there is no longer a shock present inside the nozzle, which is denoted by the design outlet pressure, and there is a supersonic flow (M>1) throughout the entire divergent section and at the nozzle exit.

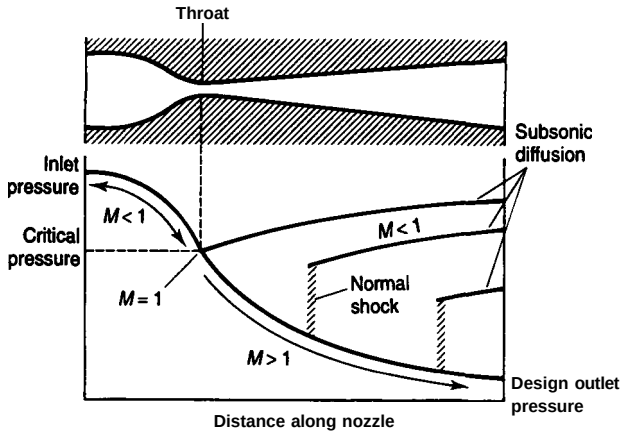

Figure 2.2: Evolution of pressure inside a convergent-divergent nozzle [29].

In CGDS, the powder particles are injected axially in the nozzle in a separate gas supply. The particles are then accelerated in the supersonic gas flow inside the nozzle, although the particles themselves do not reach sonic velocity relative to the gas flow. Particles typically range in size between 5 |am and 50 jxm, as larger particles may be too heavy to

be accelerated enough to reach the velocity required to form a coating while smaller particles may be too light and could decelerate substantially after passing through a Shockwave, thus loosing too much velocity. The particle exit velocity has been established to be a function of many parameters, as seen in equation (2.2), where V is the relative velocity between the gas flow and particle, Cd is the particle drag factor, A_p particle projected area, p gas density, x distance accelerated and m particle mass [26].

$$V_p = V\sqrt{\frac{C_d A_p \rho x}{m}} \qquad \text{...(2.2)}$$

Varying one or many parameters simultaneously can increase particle velocity. One parameter that can be modified is the gas velocity, by selecting a lighter gas or increasing the gas temperature, as described previously. It is important to note that if the gas temperature is increased to increase the gas exit velocity, the gas density will decrease. Increasing the gas pressure, which will bring up the gas density to a higher value, can counteract this effect. Both previous statements can be verified by the perfect gas law (equation 2.3).

$$P = pRT \qquad \text{...(2.3)}$$

The drag coefficient is not so easily variable as it is largely dependant on the particle geometry. For example, particles having irregular shapes, as opposed to spherical shapes, are more likely to have a higher drag coefficient, thus accelerating to higher velocities. The particle projected area may be increasing by choosing larger particles, however this a}so increases particle mass, which has an opposite effect on the final particle velocity. It can only be said that particles having low material density will travel faster than particles

having higher densities, given they have the same particle diameter. Lastly, it is also possible to increase the length of the divergent section of the nozzle *(x)* in order to increase the duration of time which the particles are accelerated, thereby increasing the particle exit velocity.

2.2 CGDS Coating Formation

Coatings made using the CGDS process are formed as the solid powder particles are accelerated to or above a certain velocity at which the particle will plastically deform and adhere upon impact with the substrate surface. The velocity at which powder particles adhere to the surface and coating formation begins is said to be the critical velocity. The deposition efficiency (DE) is linked to the particle velocity and it refers to the portion of powder present in the coating versus the total amount of powder injected during the process. As shown in figure 2.3, the deposition efficiency of copper and aluminum particles increases as the particle velocity increases [30], The deposition efficiency is also dependant on the powder material; softer materials posses higher DE than harder materials at a given particle velocity.

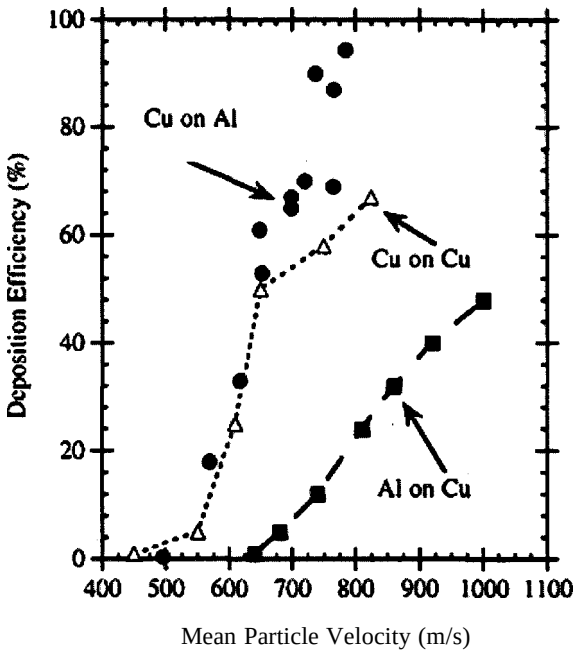

Figure 2.3: Deposition efficiency versus mean particle velocity [30J.

Although the bonding mechanism in CGDS is not completely understood to date, the most accepted theory suggests that the bonding between coating and substrate is due to a combination of plastic deformation and local shear adiabatic instabilities at the interface between the particle and substrate surface. According to the theory, the particle should acquire sufficient kinetic energy to be able to plastically deform and break the surface oxide layer, if present, on the surface of the particle and coating [27]. Upon impact, the kinetic energy is completely transformed into heat and strain energy [31]. As subsequent layers of particles build up, the underlying layer is compacted and becomes denser due to the impingement effect of the impacting particles. The plastic deformation theory is well supported by consistent results demonstrating that the CGDS process easily produces coatings of ductile materials, such as pure metals and alloys, while coatings made entirely of brittle materials like ceramics haven't successfully been produced thus far. Brittle

materials have only been incorporated into CGDS coatings by using a ductile matrix, such as metal matrix composite powder (MMC) or a composite mixture of brittle and ductile powders that were pre-mixed before injection [32, 33].

2.3 CGDS Advantages

The CGDS process has several advantages over other conventional methods, however it is the absence of melting of the powder particles that gives the process a clear advantage. The CGDS process allows the ability to produce coatings, or even parts, made of temperature sensitive materials, like nanocrystalline material, metastable alloys, or material susceptible to oxidation. It has been shown that limited or no grain growth occurs during the spraying process and that the microstructure, chemical composition and phase composition are also preserved within the coating [24]. Therefore, what is present in the feedstock powder will be present in the coating, and by engineering a new material in powder form, it is possible to engineer the coating and ultimately the part itself.

Another advantage of the CGDS process is that very little surface preparation is required on the substrate prior to spraying. Simple grit blasting has been shown to provide an adequate surface[20]. The process has also demonstrated very high deposition rates, capable of 3 mm thickness achievable in a single pass [32].

Furthermore, compressive stresses in the coating, resulting from the peening effect of the impacting particles during the CGDS process, demonstrated an increase in the fatigue resistance of the underlying part [33]. This is an advantage when compared to thermally induced tensile stresses left behind after other thermal spraying methods, due to the shrinking of the coating after cooling.

3 Experimental Procedures

Outlined in this chapter are the experimental procedures followed in this study. Sufficient detail is given that others can reproduce the results obtained and work can be continued. The experimental procedures are divided in the following main sections: alloy feedstock powder atomization, cold gas dynamic spraying facilities and process and finally, coating performance and evaluation methods.

3.1 Gas Atomization

The Al-Fe-V-Si alloy powder was prepared from individual master alloy ingots having the following respective composition: 99.75% Al, Al-25% Fe, Al-5% V and Al-36% Si. The master alloys were 7 kg waffle ingots, provided by Milward Alloys, Inc., NY, USA. Measured amounts of aluminum and master alloys were heated using an induction coil at a rate of 10°C/min until fusion. Alloying elements were added to obtain a final composition of approximately Al-5%Fe-l%V-l%Si (wt.%). This specific alloy composition was not commercially available at the time of the study, hence the reason why it was manufactured.

During the gas atomization process, high-velocity jets of gas disperse the liquid metal in a mist of fine droplets. This method increases the surface area of the molten alloy per unit volume, thus allowing higher solidification rates than other powder production methods. Atomization of the alloy powder was carried out in a high-pressure gas atomizer, where helium was used as the inert atmosphere and atomizing gas during the

process. The dynamic pressure and temperature of the atomization process were 9.4 MPa and 840°C respectively. The collected powder particles were then mechanically sieved to less than 53 fxm using a sieve shaker with wire-mesh sieves. Larger powder particles were rejected, as they may not posses the desired microstructure due to a slower cooling rate during solidification. Furthermore, larger powder particles are heavier and thus may not accelerate sufficiently to reach the critical velocity required to successfully produce a coating during the CGDS process.

3.2 Cold Spray Facility

The Al-Fe-V-Si feedstock powder alloy was sprayed onto 6061 aluminum substrate using the CGDS system developed at the University of Ottawa Cold Spray Laboratory [24, 34]. The facility consists of a fully enclosed and ventilated spraying chamber connected to two separate high-pressure gas supplies (figure 3.1). Any powder particles not adhering to the substrate during the spraying process are eventually trapped in a filtration system (shown in figure 3.2) before the exhaust flow is vented to the atmosphere. The filtration system is equipped with high-performance HEPA filters, which are 99% efficient in capturing particles as small as 1 p.m. The primary gas supply (propellant gas) is connected to a converging-diverging nozzle, shown outside the spraying chamber in figure 3.3, which generates the supersonic gas flow. A resistance-heater (figure 3.4a) positioned between the gas supply and spraying nozzle, consists of a stainless steel pipe connected to a high amperage power supply (figure 3.4b). The gas stagnation temperature

is adjusted by varying the amperage of the power supply and is monitored by a pair of thermocouples, one at the heater exit, shown in figure 3.5, and the other at nozzle entrance.

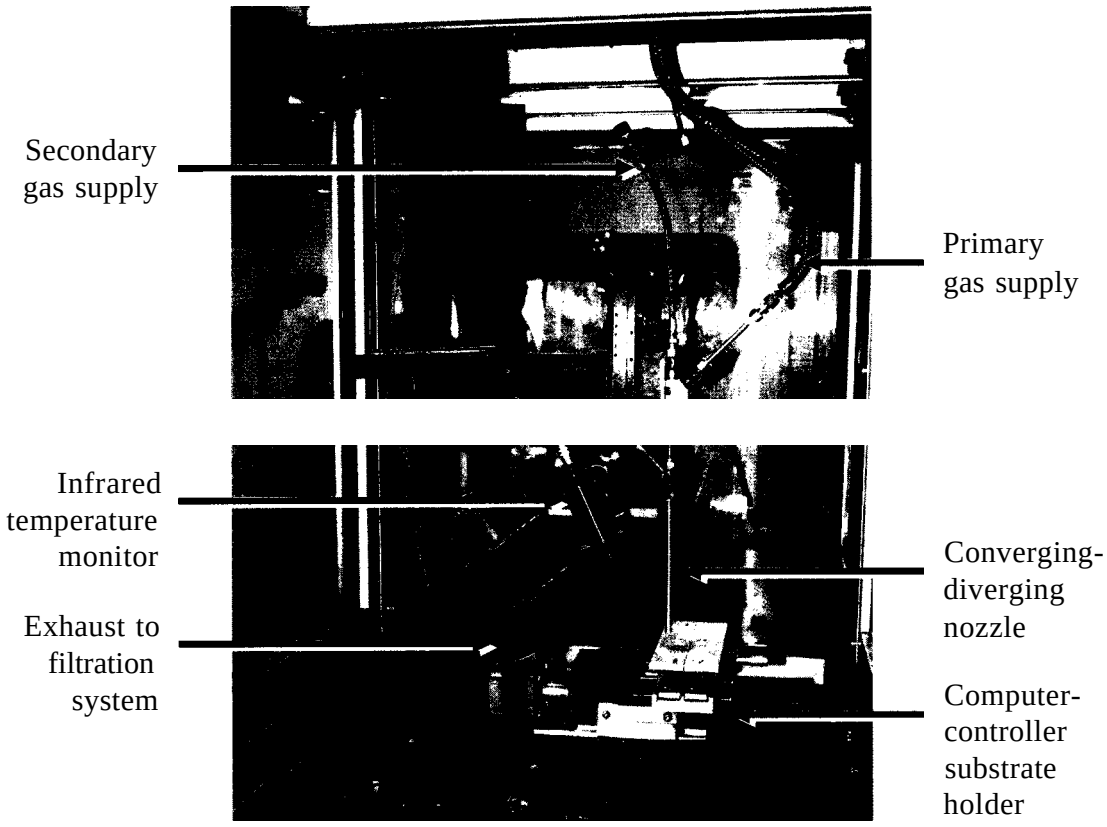

Figure 3.1: University of Ottawa CGDS Laboratory spraying chamber.

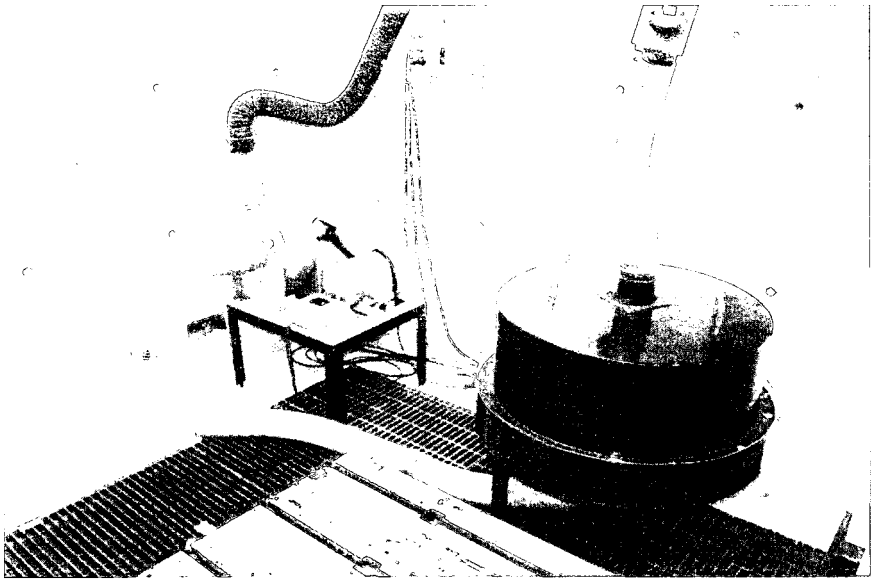

Figure 3.2: Filtration system.

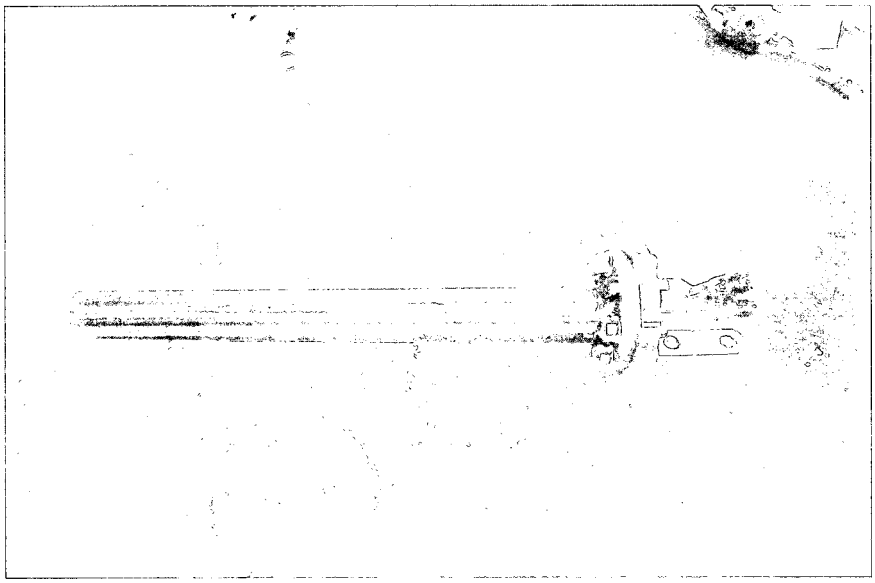

Figure 3.3: Converging-diverging nozzle.

(a) **(b)**

Figure 3.4: Resistance heater coil (a) and power supply (b).

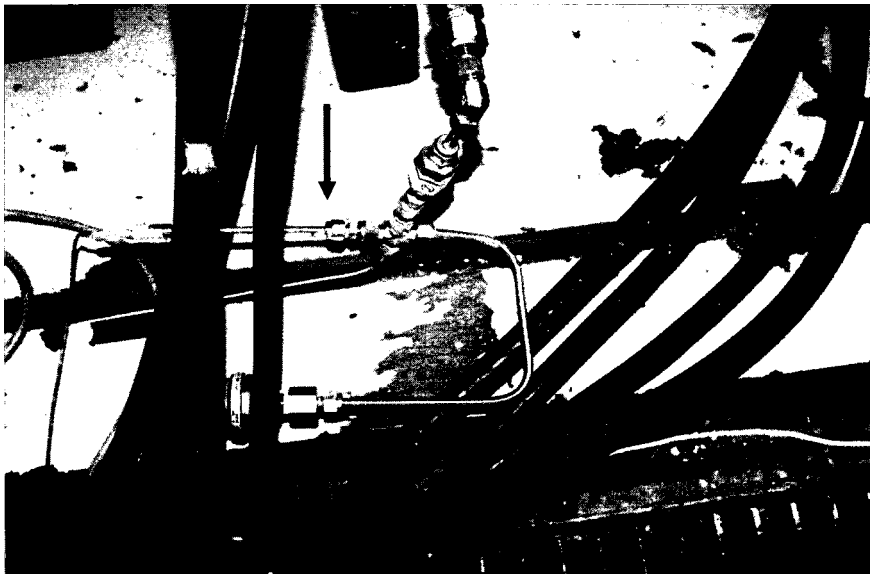

Figure 3.5: Thermocouple measuring heater gas exit temperature.

A commercially available powder feeder (Praxair model 1264), seen in figure 3.6, was modified for this study to withstand higher internal pressure than its original design. A secondary gas supply (feeding gas) is connected to the powder feeder in order to pressurize the unit, which in turn injects the powder particles axially at the entrance of the nozzle. The powder feeder is also equipped with an adjustable feed-rate controller that allows the injection of feedstock powder at a constant mass flow rate. The spraying chamber is fitted with an infrared (IR) temperature monitoring system (figure 3.1), which continuously measures the temperature of the coating and substrate. The substrate/coating temperature is monitored in order to ensure the microstructure of the coating will not be affected. Finally, a computer-controlled substrate holder enables movement in an X-Y plane enabling coating of a planar surface. System parameters, such as static pressure and stagnation temperature of the propellant gas are measured at the entrance of the converging-diverging nozzle and are recorded in a data acquisition system, which is shared with the substrate holder controller.

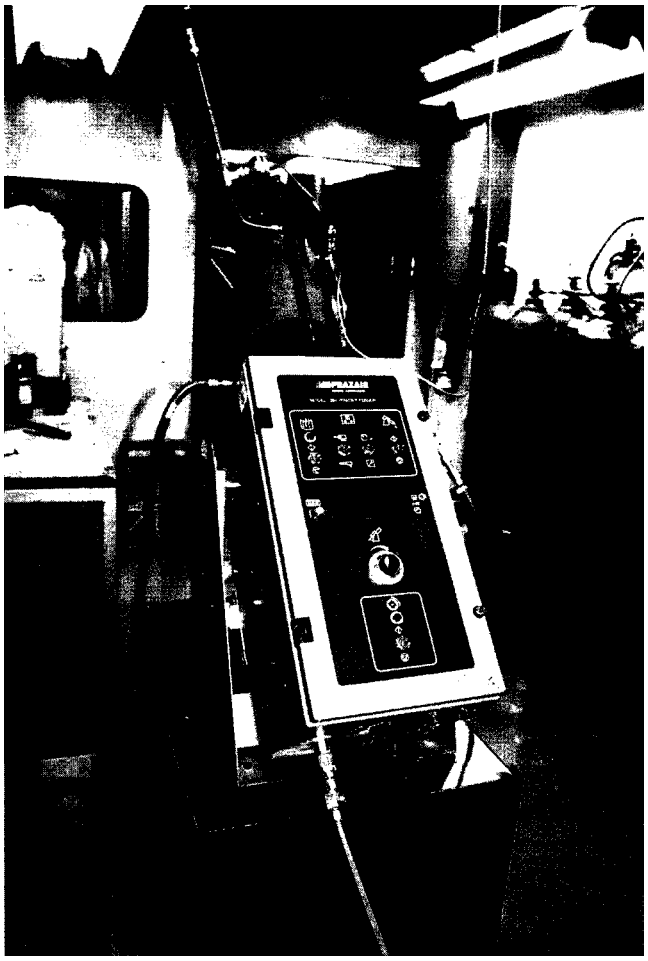

Figure 3.6: Modified Praxair model 1264 powder feeder.

The spraying parameters were determined from simulations of the spraying process using a validated numerical model [24]. The model estimates the gas and particle velocities to ensure that critical velocity is reached in order to form a coating. The model can also determine if any shockwaves are present in the flow, and if so, their position with respect to the nozzle exit plane. Helium and nitrogen were separately used as the propellant gas in this study, both at a stagnation pressure and temperature of 1 MPa and 250°C respectively. It is expected that the feedstock powder particles will travel at lower velocities when using nitrogen rather than helium due to its aerodynamic properties. For a

given nozzle Mach number design, nitrogen reaches a lower velocity than helium, mainly due to its higher atomic weight. Therefore, the powder particles may not reach the critical velocity required to produce a coating when the latter gas is used. One method to overcome this is to introduce hard powder particles in the feedstock powder to increase deformation through impingement of the harder particles impacting the softer layer of the feedstock powder particles. However, it is expected that this practice may result entrapment of the hard particles in the coating, resulting in a composite coating [35].

A nozzle stand-off distance of 10 mm and a nozzle exit diameter of 7.8 mm were used and kept constant for a given set of experiments in order to ensure repeatability for different trials. The operating spray parameters consisted of a single gun pass, using a traverse velocity of 2 mm/s. However, the coating of bond strength specimens required multiple overlapping passes to completely cover the sample surface.

3.3 Substrate Preparation

The substrates were cut from commercial Al-6061 6.35 mm thick bars before being subjected to a specific surface preparation. It has been shown that simple media blasting is sufficient to prepare the surface for the CGDS process [20]. For this study, the substrate was grit blasted using silica (quartz) beads having an average particle diameter of 686 jam (20 mesh - 24 grit). This method of surface preparation is generally accepted as providing enough substrate surface roughness to promote the mechanical interlocking bonding mechanism at the particle-substrate interface without having any significant effects on the coating microstructure [20].

3.4 Powder and Coating Evaluation

3.4.1 Scanning Electron Microscopy

The scanning electron microscope functions by aiming a beam of electrons towards the sample, the electrons that bounce off the sample are then collected and analyzed. Their energy is quantified and used to create an image. This imaging mode is called Back-Scattered Electron (BSE) imaging. The BSE energy is linked to the atomic number, therefore this imaging mode is mostly used to identify different chemical compositions within the sample through image contrast ratios. The electron beam also causes electrons belonging to the sample to be ejected from their orbit, which are called Secondary Electrons (SE), and their information is also used to for imaging.

Powder samples were mounted in resin, followed by standard metallographic grinding and polishing procedures prior to SEM observation. Scanning Electron Microscopy was carried out to determine the powder morphology and its general microstructural characteristics using a Philips XL30 FEG SEM, operating in both SE and BSE modes.

To evaluate the coatings, cross-sections were cut using a Struers Secotom-10 water-cooled saw (figure 3.7) equipped with a 203 mm alumina blade, operating at 3000 rpm and advancing at 0.5 mm/s. The cross-sections were then mounted in Struers MultiFast Green phenolic hot mounting resin using Struers LaboPress-3 equipment (figure 3.8), according to the manufacturer's suggested mounting parameters. Grinding and polishing

was done on a Struers TegraPol-31 machine with a TegraForce-5 specimen mover, equipped with a TegraDoser-5 fully programmable system (shown in figure 3.9), which controls the polishing fluid application, polishing time and polishing force. The grinding and polishing sequence was based on standard metallographic procedures and adjusted for the substrate and coating alloy combination. Final polishing ended with a 2 minutes and 20 seconds cycle using a 1 (j.m diamond suspension.

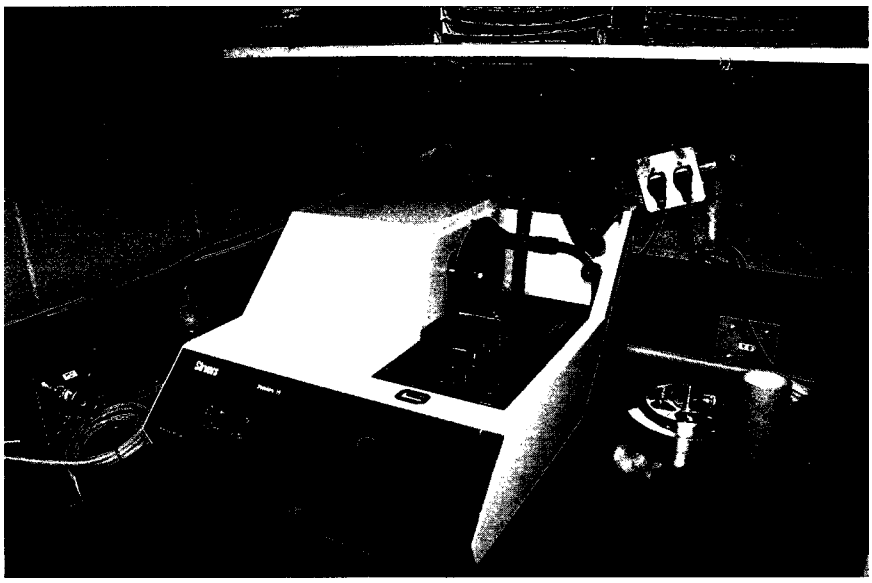

Figure 3.1: Struers Secotom-10 water-cooled saw.

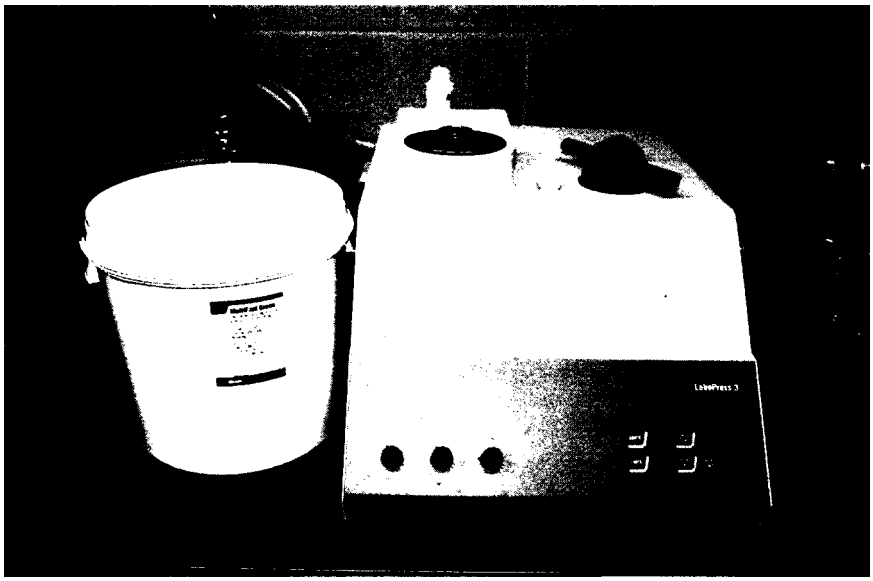

Figure 3.8: Struers LaboPress-3 mounting press.

Figure 3.9: Struers TegraPol-31 grinding and polishing machine, TegraForce-5 specimen mover, and TegraDoser-5 polishing system.

Coatings were examined under SEM to determine porosity level and inter-lamellar cracking occurrences. The porosity level was evaluated using a commercial image-

processing software, Clemex vision-Lite, where a grayscale threshold was applied to the digitized coating cross-section images and the surface fraction of porosity was subsequently compiled. Volume fraction of hard-particles in the composite coatings produced using nitrogen as the propellant gas was also calculated in a similar fashion.

3.4.2 Transmission Electron Microscopy

In a transmission electron microscope, electrons are fired at a very thin sample. The electrons pass through the sample and are projected on a phosphorescent screen, where an image can be seen. The TEM operates in three basic modes: Bright-Field (BF), Dark-Field (DF) and Selected Area Electron Diffraction (SAED). Bright-field refers to the image created from the electrons which travel through the sample, whereas dark-field refers to the image formed from the electrons that are deflected at the same angle while traversing the sample. SAED mode forms an image of the pattern created by all the deflected electrons traversing a selected area of the sample. The SAED pattern is used to identify the phases present in the sample by measuring the distance between the diffraction spots (or rings). The information can then be correlated to the distance between atomic planes, which is specific to each phase. Finally, X-rays, which are also emitted from the sample as it is bombarded with the electron beam, reveals information on the elemental composition of the sample.

The Al-alloy powder particles were mounted in 3 mm hollow brass tubes using Gatan-Gl epoxy. The tubes were set vertically on a hot-plate in order to decrease the setting time to roughly 5 minutes at 65°C. The tubes were cut into disk and hand sanded to a thickness

of approximately 100 |jm. A Fischione model 200 dimpling grinder (figure 3.10) was used to create a dimple (or crater) to achieve a thickness of about 10 (j.m in the center of the disk, in order to reduce final polishing time. Finally, the sample was ion-milled in a Fischione Model 1010 Low angle ion-milling and polishing system (figure 3.11) using argon gas and operating at 3 keV, 3 mA and a 15° milling angle for 2 hours, followed by a 12° milling angle until a laser light threshold system detected a hole in the sample. At the edge of the hole, the sample is very thin due to the very shallow milling angle. The sample must be less than one hundred nanometres in thickness for the electrons to traverse the sample without being deflected substantially in order to produce a clear image. For high-resolution TEM, the sample must be even thinner, in the order of a few nanometres, to clearly see the atomic planes.

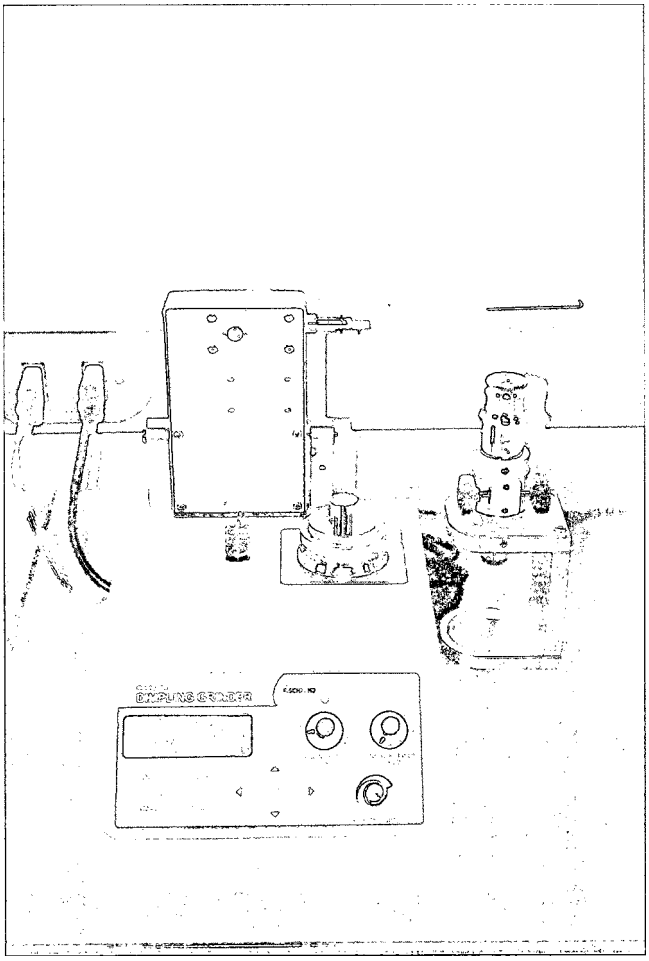

Figure 3.10: Fischione model 200 dimpling grinder.

Figure 3.11: Fischione model 1010 low angle ion-milling and polishing system.

The coating samples were prepared by completely and carefully removing the aluminum substrate by manual sanding. The coating was further sanded until a thickness of 100 (j,m was achieved and a 3 mm disk was punched using a hand punch. Dimpling and ion-milling procedures that followed thereafter were similar to those outlined for the powder samples preparation.

The microstructural investigation was performed using a FEI Tecnai-G2 F20 High-Resolution Transmission Electron Microscope (HRTEM) operating at 200 kV (figure 3.12). The latter is equipped with an Energy Dispersive Spectroscopy (EDS) ED AX system for chemical composition analysis. During EDS analysis, enough collection time was allowed to reach at least 6000 counts to ensure representative values of atomic composition and avoiding false readings. Different modes of observation were used such

as Bright-Field (BF) and Dark-Field (DF), as well as Selected Area Electron Diffraction (SAED) for phase identification. FEI digital imaging software allowed for image processing such as direct SAED pattern indexing.

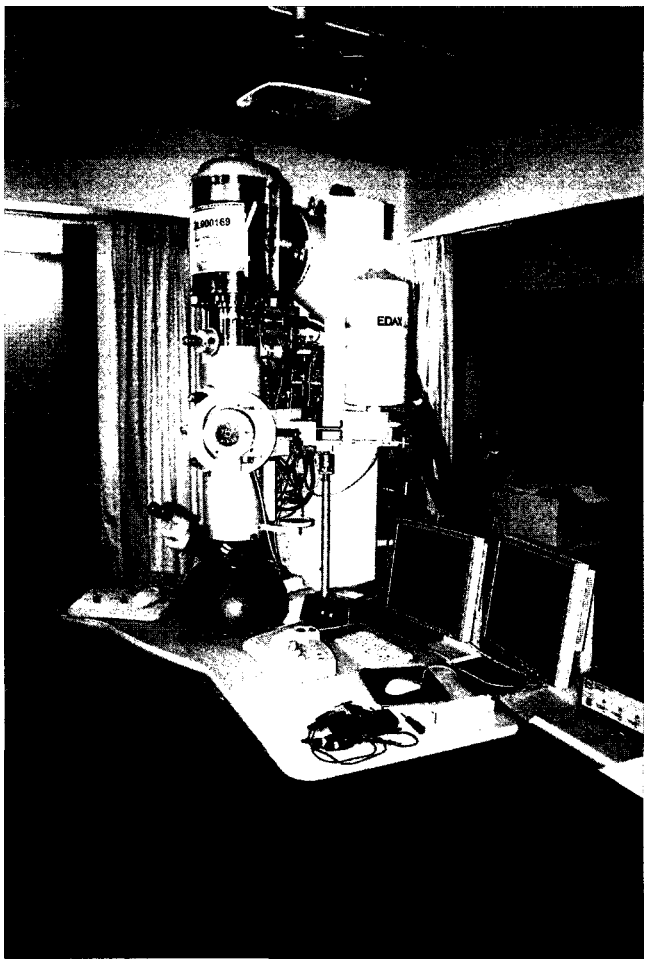

Figure 3.12: FEI Tecnai-G2 F20 high-resolution transmission electron microscope.

3.4.3 Differential Scanning Calorimetry

A differential scanning calorimetry apparatus works by recording the heat input that is required to heat a sample at a linear temperature increase over time. A separate control

sample is heated at the same rate and its heat input also recorded. The differential heat input between both samples is then plotted as a function of temperature and any peak in the curve indicates a change in microstructure or phase changes. The thermal stability of the Al-Fe-V-Si alloy was determined using a Differential Scanning Calorimetric (DSC) TA Instruments Q20 machine. A 32.2 mg powder sample was scanned at a temperature range of 40°C to 580°C with a heating rate of 10°C per minute.

3.4.4 X-Ray Diffraction

X-ray diffraction is an investigative technique, which is used to retrieve information about the crystallographic structure, chemical composition and phase identification by collecting scattered intensity and scattering angle of an X-ray beam directed at a small sample. The results are plotted as a function of the scattering angle and compared to a database of diffraction plots of known elements and compounds. The XRD analyses were carried out in a Philips X-Pert model 1830 X-ray diffractometer, illustrated in figure 3.13, using Cu Ka *(X=0.*15406 nm) radiation, 20-50° 20 range, 0.01° step width, and 2 s per step acquisition time.

Figure 3.13: Philips X-Pert model 1830 X-Ray diffractometer.

3.5 Aging

3.5.1 Controlled Aging

Aging was performed to assess the thermal stability of the metastable alloy coating at elevated temperatures. Sections of substrates and coatings were placed in a temperature controlled air furnace, shown in figure 3.14, at 400°C. The samples were taken out after 96 hours. This temperature was chosen to represent the highest temperature at which the coating would be exposed in an IC gasoline engine.

Figure 3.14: Temperature controlled air-furnace.

3.5.2 In-Situ Accelerated Aging

In-situ accelerated aging of a coating sprayed on an engine piston head was conducted on an 8-cylinder gasoline engine, running for approximately 300 hours to represent the performance of the coating in real-life condition. The piston was subsequently removed and cut into cross-section and prepared using standard metallographic procedures.

3.6 Mechanical Properties

3.6.1 Adhesion Strength Testing

The bonding strength of the coatings to the substrate surface was assessed by performing the ASTM standard C633-01 [36]. This test is used to determine if the sample will fail and delaminate during its normal operational conditions. The standardized bond sample substrates were prepared from the same commercial alloy than the coating substrates, using the same surface preparation as described above. Spraying parameters were also kept constant for a given test in order to correlate the results to the analyses obtained from imaging.

Coatings were sprayed onto cylindrical substrates with multiple overlapping passes to completely cover the surface, as illustrated in figure 3.15. The coating was then machined on a lathe to ensure the surface is entirely smooth, flat, and also normal to the tension force applied during testing. Master Bond EP15 epoxy was applied to the machined coating surface and mated to an identical cylindrical substrate, but without coating. An alignment jig was used to apply light pressure and maintain alignment during curing, according to the time and temperature specified by the manufacturer. The tensile strength was obtained from an Instron model 4482 tensile testing machine (figure 3.16), operating at constant displacement rate. The tension force was recorded at the point of rupture of the sample specimen. At least three samples were tested to get an average value of the coating adhesion strength. The failure mode was also determined according to the standard.

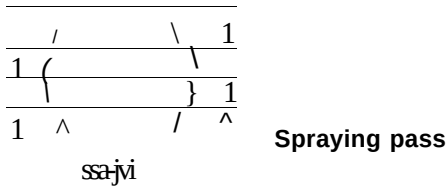

Figure 3.15: Schematic representation of multiple overlapping passes.

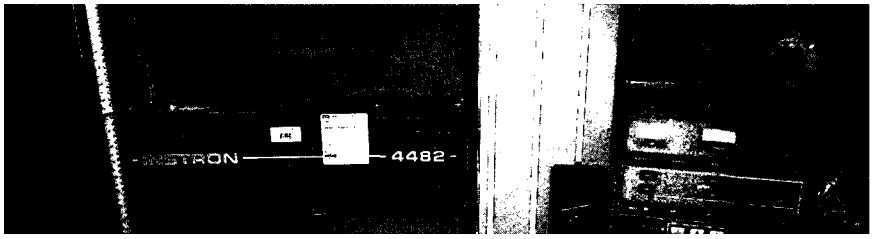

Figure 3.16: Instron model 4482 tensile testing machine.

3.6.2 Microhardess Measurements

Microhardness was evaluated on polished coating samples using Struers Duramin equipment, seen in figure 3.17, equipped with a Vickers indenter, using a 300 grams weight applied for 10 seconds. The microhardness results can be used to approximate the tensile strength of the coating, or such as in this case, modifications to the yield strength after undergoing aging. Ten measurements were taken on each specimen to ensure a

representative value of microhardness. Each individual measurement was taken at least three indentation diameters from a previous measurement to ensure that the readings are not affected by the work hardening done by the previous indentations marks.

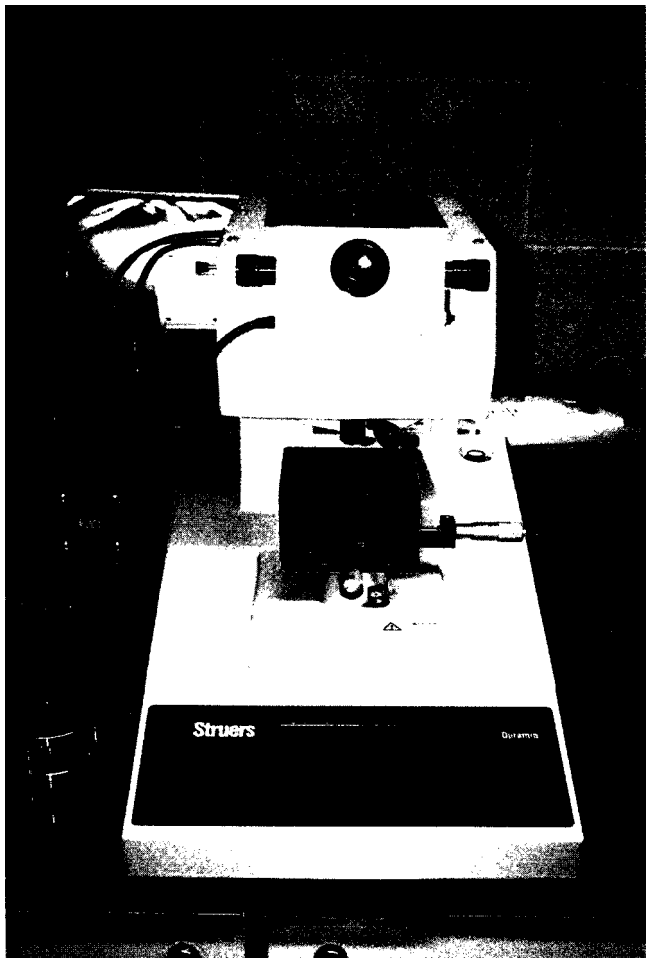

Figure 3.17: Struers Duramin microhardness testing machine.

3.7 Particle Velocity Measurements

Critical velocity is often referred to in the CGDS process and is usually defined as being the velocity at which deposition occurs and an appreciable coating thickness is achieved

[37]. Many spraying parameters can have a direct impact on the particle velocity, and thus the resulting coating properties [28]. Therefore, the particle velocity is often monitored to ensure repeatability and consistency between experiments. Measurements were taken at the nozzle exit plane at the center of the gas jet. Particle velocity data was collected using a laser particle diagnostic system, a Cold Spray Meter by Tecnar Automation Ltd. The unit functions by illuminating an interrogation volume using a continuous laser light source. An optical lens fitted with a dual-slit photo mask captures the reflection of the moving particles. The signal is then amplified, filtered and analyzed by the data acquisition system. A simplified schematic representation of the photo mask and signal is illustrated in figure 3.18, while the actual measurement head and placement can be seen in figure 3.19. A computer algorithm correlates the time difference between two identical peaks, since the distance between the slits is known, the velocity can be calculated [38],

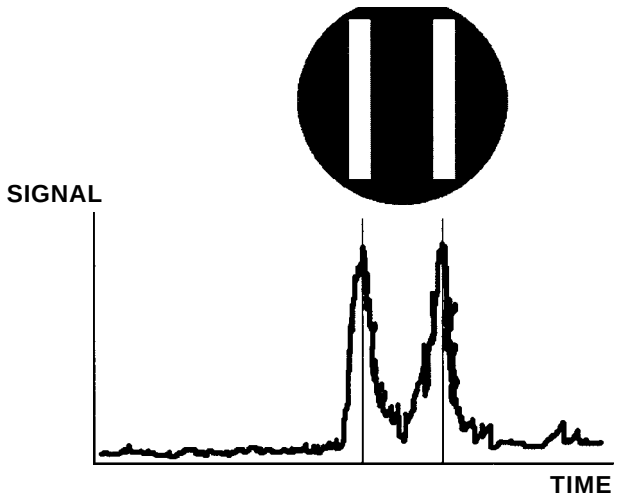

Figure 3.18: Cold Spray Meter schematic representation.

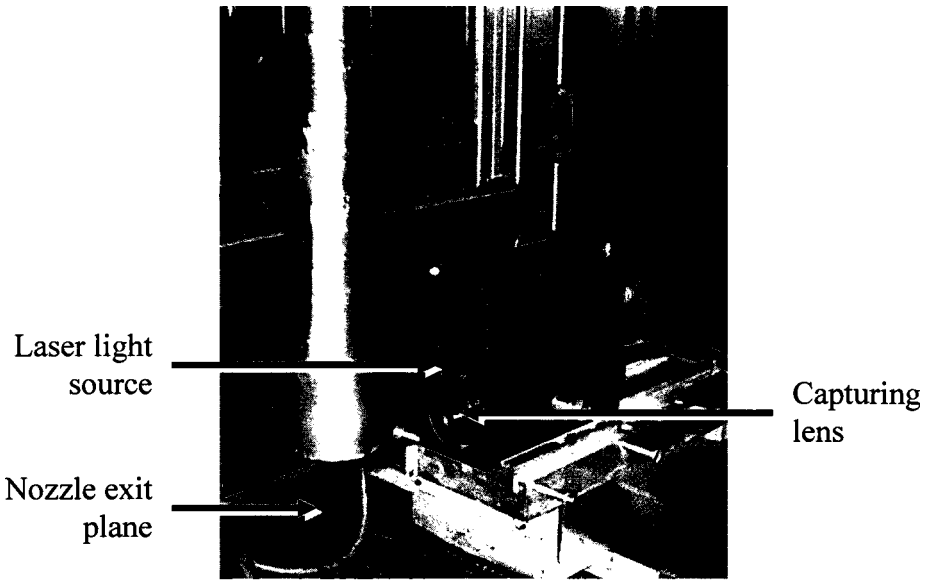

Figure 3.19: Cold Spray Meter measurement head.

4 Results and Discussion

In this section, the results pertaining to the atomized Al-Fe-V-Si alloy powder, Al-alloy coatings and composite coatings are presented and discussed. General microstructural observations, phase identification and thermal stability of the feedstock powder and coatings produced are presented first, followed by selected coating performance, which was evaluated in terms of porosity, adhesion strength and microhardness.

4.1 Powder

During the atomization process, the unusually high viscosity of the molten Al-Fe-V-Si alloy made it difficult to atomize adequately. The atomizing pressure and temperature were therefore increased to values higher than those typically used for atomization of aluminum powders. The increased viscosity is most likely due to the high concentration of the alloying elements. Following atomization, the collected powder particles were sieved to less than 53 jxm, which resulted in an overall process yield of 55% by mass. However, it is envisioned that the rejected powder particles can be reused in a subsequent atomization run by re-melting and mixing with the Al-alloy, thereby increasing the overall process yield.

4.1.1 Powder Morphology

The general morphology of the Al-Fe-V-Si alloy powder produced by gas atomization is shown in figure 4.1, an SEM image of the as-atomized powder. It can be observed that the powder particles have a spherical morphology, with a size ranging from approximately 5 }im to 60 (im in diameter. It can also be noted that satellites of smaller diameter particles (1 |im to 10 |j.m in diameter) formed and agglomerated to larger particles during solidification giving an irregular shape to the resulting powder particles. Higher drag coefficients are often associated with irregular shaped particles compared to spherical particles. Therefore, it is expected that the irregular-shaped particles will accelerate over a shorter distance and reach higher velocity at the nozzle exit than spherical ones [39].

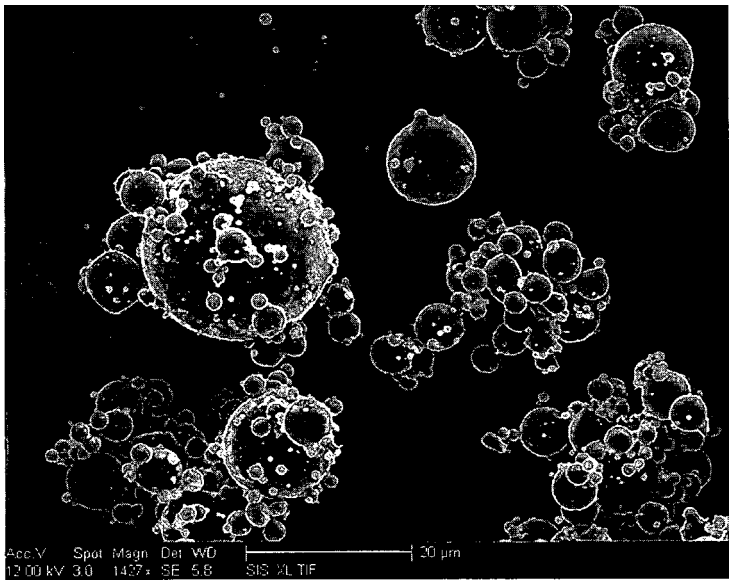

Figure 4.1: SEM image of the as-atomized Al-Fe-V-Si alloy.

4.1.2 Powder Microstructure

The microstructure of the as-atomized powder particles is shown in figure 4.2, an SEM image of the cross section of a single distinct powder particle at higher magnification. The image reveals that the microstructure of the Al-alloy is composed of different regions where various nucleation sites with arm-shaped structures radiate outwards.

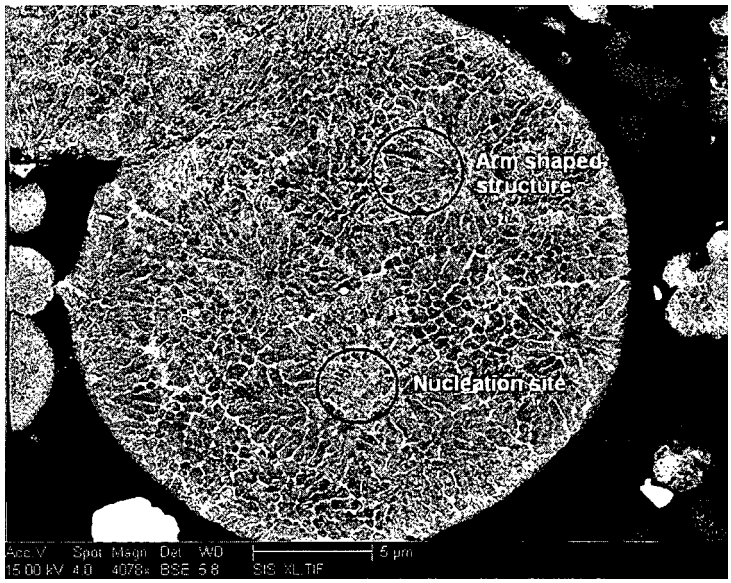

Figure 4.2: SEM image of a single distinct powder particle.

The observed microstructure in the as-atomized Al-Fe-V-Si powder particles varies slightly according to the particle size, most likely resulting from differences in the cooling rate during solidification. In gas atomization, solidification is governed by very high convection cooling rates. An important parameter of this cooling process is the Biot number, which is a measure of the temperature drop inside the object relative to the

temperature difference between its surface and the fluid environment. As shown in equation (4.1), the Biot number is function of the convection heat transfer coefficient *h*, the diameter of the particle *D* and the thermal conductivity *k* of the material. Therefore, the resulting cooling rate, and solidification of the particle is directly linked to its diameter and ultimately the particle's microstructure is also dictated by its diameter.

« - f …(4.1)

In general, TEM observations of the as-atomized powder revealed three different regions, schematically illustrated in figure 4.3. One region consists of very fine precipitates homogeneously distributed in the Al-matrix, hereafter named "zone A". The second region, identified as "zone B", is characterized by a typical microcellular structure, with elongated arm-shaped grains. A coarser, more equiaxed microstructure also containing larger precipitates is identified as "zone C". These names are homologous to those used in the work of Tongsri *et al* [40],

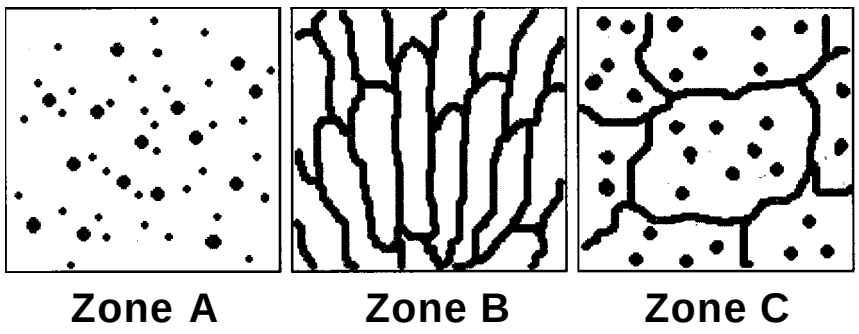

Figure 4.3: Schematic representation of distinctive microstructural zones.

The BF-TEM image shown in figure 4.4 illustrates a general view of the as-atomized powder particles. The image shows one large powder particle in the centre, with two smaller satellite powder particles on the left and another one on the bottom. It can be observed that the two smaller powder particles on the left appear to have a similar microstructure but different than that observed in the largest central powder particle. Detail of the microstructure of one of the satellite powder particles of figure 4.4 is shown at a higher magnification in figure 4.5. From this figure, it can be concluded that the small satellite powder particle only exhibits "zone A" and "zone B" microstructures, as indicated in figure 4.5. In the bottom third portion of the satellite powder particle, the microstructure is composed of fine precipitates distributed in a homogenous Al-matrix (zone A). A transition into an arm-shaped microcellular region is observed right above "zone A" until the microstructure is entirely composed of "zone B" in the upper third portion.

0.5 Mm

Figure 4.4: Bright-field TEM image of Al-Fe-V-Si powder particles showing one large particle with three satellites and their microstructure.

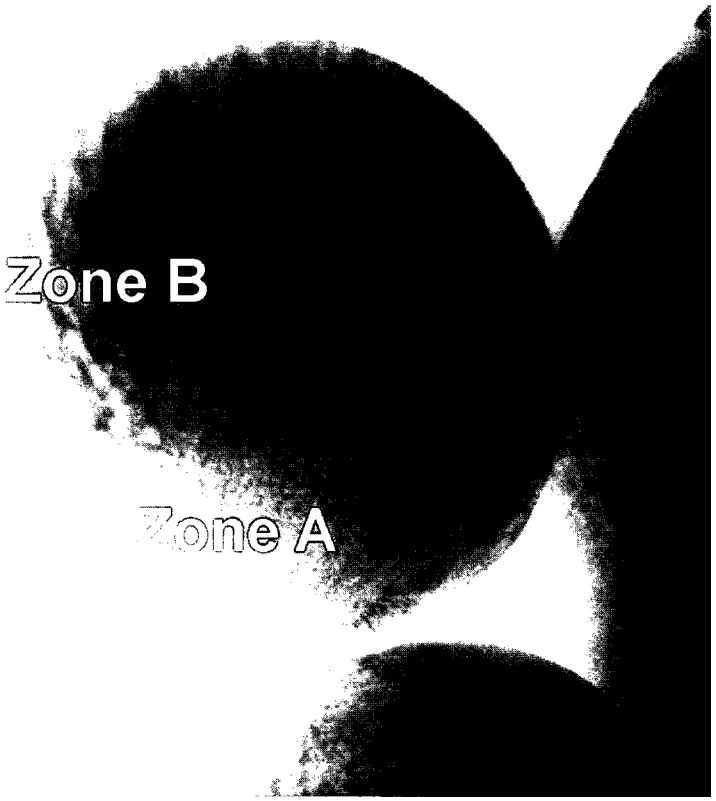

Figure 4.5: Bright-field TEM image showing microstructural details of the smaller powder particle, illustrating the transition from "zone A" to "zone B".

Figure 4.6 is an SAED pattern obtained from the entire satellite powder particle shown in figure 4.5. The diffraction pattern contains sharp diffraction spots, which are due to the crystalline aluminum matrix. Ring patterns are also observed in the diffraction pattern and may indicate the presence of a very fine grain microstructure, or amorphous phase. However, the rings do not appear diffuse enough to confirm the presence of an amorphous phase. As such, the ring possessing the highest intensity was used for DF imaging to further investigate where this phase occurs in the powder particle of figure 4.5. The DF image shown in figure 4.7 illustrates that the ring is due to the precipitates

present in "zone A" and also the intercellular region of "zone B". Therefore both regions are most likely composed of the same phase since they possess a similar intensity in the image. A previous study suggests that the fine precipitates and intercellular region are composed of a micro-quasicrytalline icosahedral (MI or QC) phase, which is coherent with the presence of rings in the SAED pattern due to the quasicrystalline microstrucutre. According to the work by Tongsri [40], the MI phase is composed of very fine nano-sized quasicrystals.

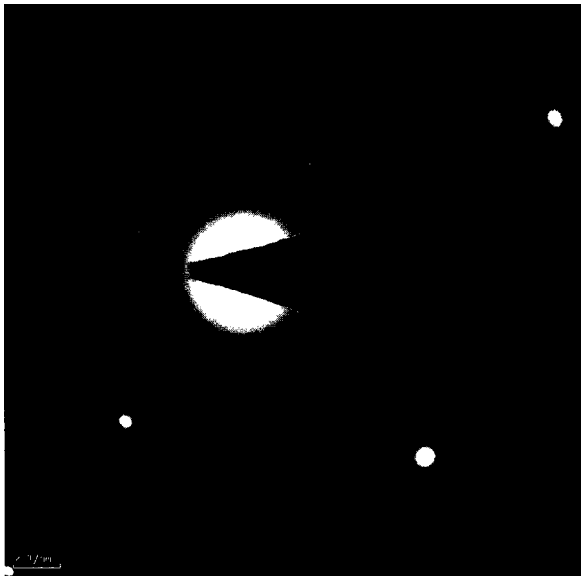

Figure 4.6: SAED Pattern of the larger powder particle shown in Figure 4.5.

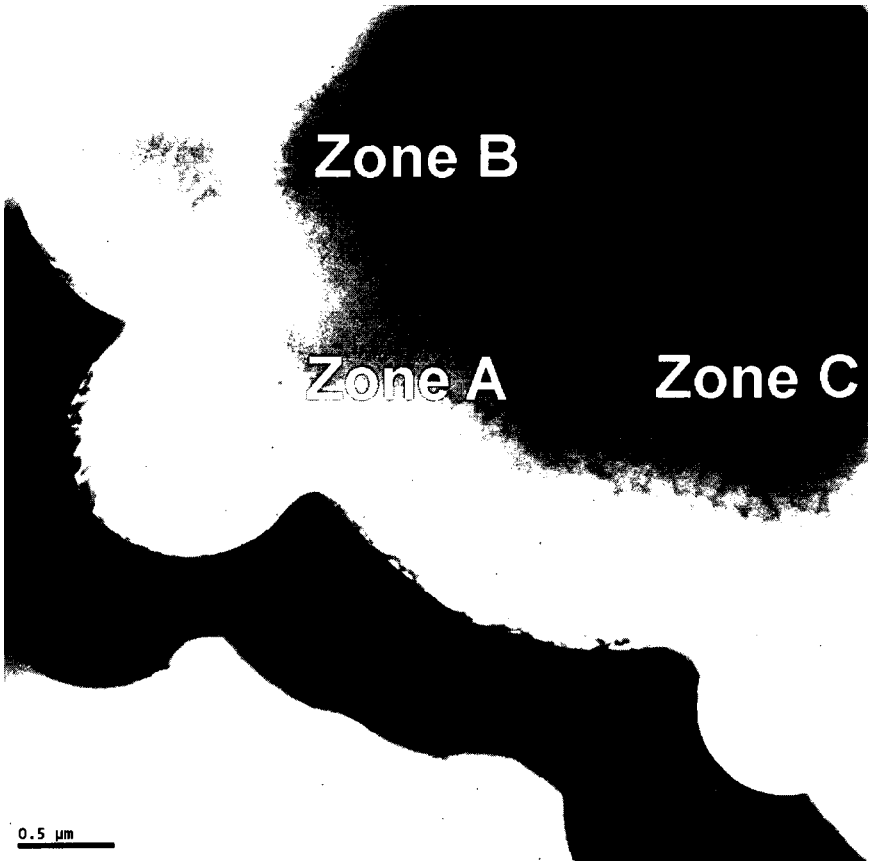

Figure 4.7: Dark-field TEM image illustrating the precipitates and intercellular phases.

The largest of the powder particles of figure 4.7 contains "zones" A and B in the left side of the particle and "zone C" in the remainder of the particle. "Zone C" is not present in the smaller satellite particles previously discussed. Highlighted in figure 4.7, it can be noted that the microstructure adopts a coarser more equiaxed grain structure with darker shaded grain boundaries where "zone C" exists. The lower section of this powder particle is magnified in the DF image of figure 4.8. Again, finely distributed precipitates within the grains of "zone C" exhibit strong diffraction intensity in the DF image, which suggests they are composed of the same phase as found in zones A and B. It can also be observed that the intercellular region of "zone C" does not diffract in the DF image,

suggesting the presence of a different phase than that of the precipitates in "zone A" and the intercellular region of "zone B". It is speculated that this new phase is a silicide phase as suggested in previous studies [40]. Therefore, "zone C" is presumably composed of finely distributed Mi-phase precipitates in the matrix, while the silicide phase only appears to be present at the grain boundaries.

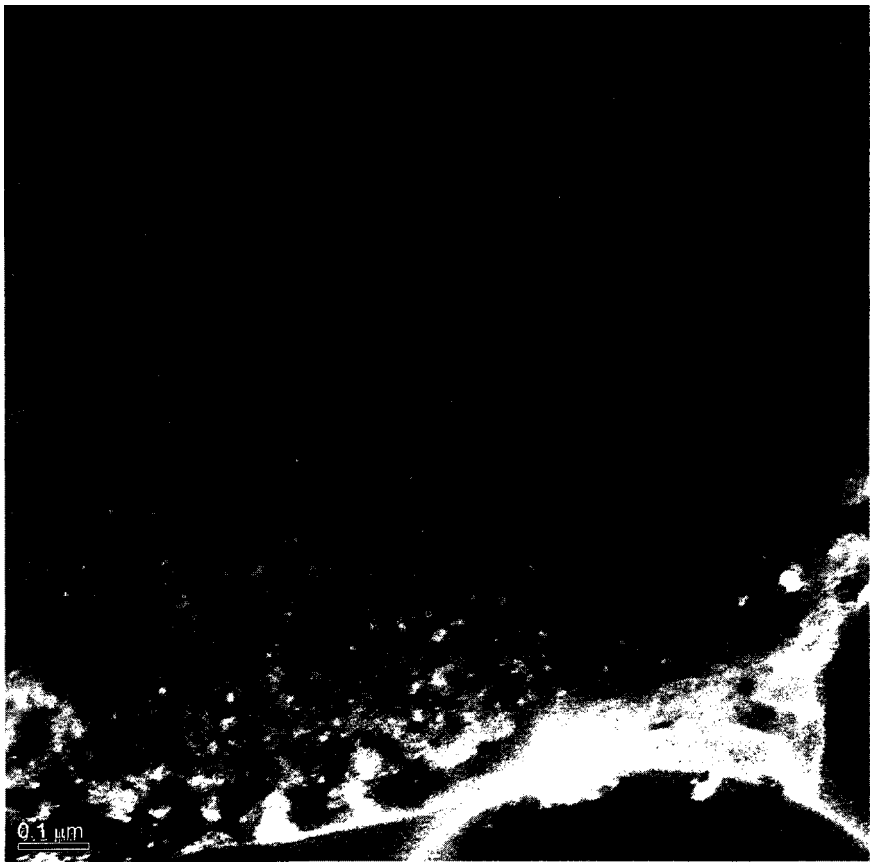

Figure 4.8: Dark-field TEM image demonstrating the presence of two different phases in "Zone C".

The microstructural development of the different "zones" within the powder particles may be explained using the following assumption. During solidification, suspended

intermetallic particles are either pushed or engulfed by the solidification front, depending on the size of the intermetallic particles and velocity of the solidification front [40]. Under this assumption, "zone A" is formed as intermetallic particles grow while suspended in the liquid a-aluminum matrix. After nucleation, the a-aluminum solidification front travels at very high velocities and engulfs the intermallic particles. "Zone B" is formed when the solidification front velocity begins to slow down and a cellular front develops. At this time, the intermetallic particles are pushed aside and entrapped in the intercellular region. Finally, in "zone C", it is assumed that the solidification front velocity has decreased even further to a coarse cellular or dendritic front, which allows the intermetallic particles to grow further in size before solidification of the matrix. This may explain why "zone C" is only present in larger particles, since their solidification time is greater than that of smaller particles and also the same reason why intermetallic particles in "zone C" are larger in diameter than those in "zones" A and B.

4.1.3 Phase Identification

The XRD data and ring pattern indexing data from the TEM observations are shown in Table 4.1, where the a-aluminum peaks were excluded. XRD was conducted to demonstrate that the phases identified locally using TEM are also present in the bulk of the powder due to the larger sample size analyzed during XRD. The observed d-spacing, analogous to the spacing between atomic planes in a material's crystalline structure, were compared to those from the Joint Committee on Powder Diffraction Standards (JCPDS) numbers 6-669, 44-1195 and 51-1193. Figure 4.9 illustrates the XRD scan of the as-

atomized Al-Fe-V-Si powder, while the diffraction angles were converted into ^-spacing in Table 4.1. The <i-spacing values indicate the presence of two different phases, namely the micro-quasicrystalline icosahedral (Ml) phase and the silicide phase, coherent with the TEM deductions. The observed ^-spacing measured from the electron diffraction pattern of the powder particles compare well to those from the XRD pattern. The silicide phase referred to was determined as the bcc Ali3(Fe,V)3Si, after comparison with JCPDS values and results from Tongsri [40].

TABLE 4.1 Possible phases of the Al-Fe-V-Si powder by XRD and SAED indexing.

XRD d-spacing (nm)	SAED indexing ^-spacing (nm)	Possible phase
	0.406	Silicide $Ali_3(Fe,V)_3Si$
0.396		Silidide
0.253	0.251	Silicide
0.235	0.235	Silicide
0.207	**0.206**	Silicide + Ml $(Al,Si)_x(Fe,V)$
0.203	0.203	Silicide + MI $(Al,Si)_x(Fe,V)$

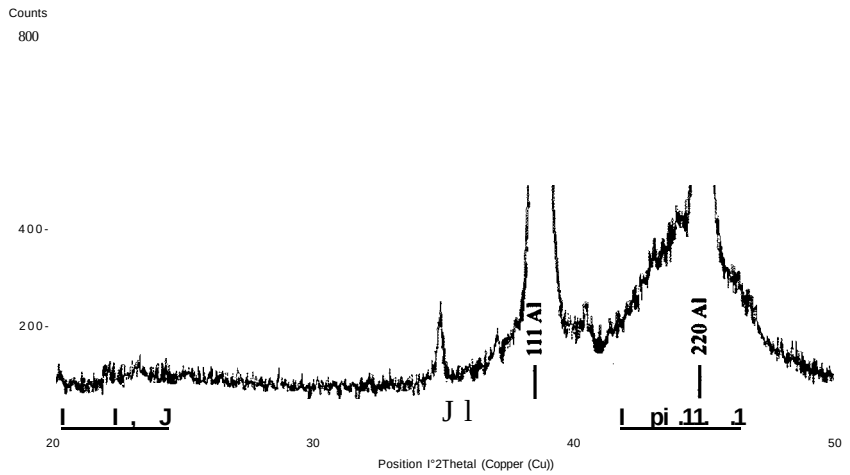

Figure 4.9: XRD pattern of the Al-Fe-V-Si powder. Other than the Al main phase, the pattern shows the presence of small reflections due to the presence of the Ali3(Fe, V)sSi and (Al,Si)$_x$(Fe, V) phases.

Phase composition was supported by EDS analysis, where the chemical composition for the silicide and MI phases are tabulated in Table 4.2. It was determined that the MI phase composition was (Al,Si)^(Fe,V), where *x* is in the range of 6 to 7. Due to the thickness of the sample, there is a significant amount of a-aluminum matrix surrounding the analyzed particle, therefore resulting in a high atomic percentage of aluminum within the tabulated values. However, the actual atomic percentage ratio between the other alloying elements (Fe, V and Si) does match that of the identified phases.

TABLE 4.2 EDS atomic composition of identified phases.

Element	$Ali_3(Fe,V)_3Si$	$(Al,Si)_x(Fe,V)$
A1	94.59 %	96.15%
Fe	4.15%	2.99%
V	0.23 %	0.23 %
Si	1.02%	0.62%

4.1.4 Thermal Stability

The microstructural stability of the Al-Fe-V-Si powder was evaluated using Differential Scanning Calorimetry (DSC) in the temperature range of 40°C to 580°C with a heating rate of 10°C per minute. The DSC curve shown in figure 4.10 demonstrates only one notable exothermic peak at around 420°C, which initiates at approximately 380°C. The exothermic peak may be attributed to the simultaneous transformation of both phases identified in the previous section, however it is most likely that it is due to the transformation of the $(Al,Si)_x(Fe,V)$ MI phase into the more stable $Ali_3(Fe,V)_3Si$ silicide phase. Further TEM investigation would need to be done on samples exposed to temperatures above the exothermic peak temperature to confirm the hypothesis of this phase transformation. If such is the case, it can be said that the metastable Al-Fe-V-Si alloy powder loses its MI phase to a silicide phase and thus its desired properties when exposed to temperatures above 380°C. This shows that the alloy is indeed a good candidate for the CGDS process as the particles are never exposed to such temperature during spraying and therefore the microstructure should be preserved within the as-

sprayed coatings. It can be expected that parts coated or fabricated from this alloy could operate safely at temperatures above 350°C, without any phase transformation or phase loss. The DSC analysis demonstrated that the metastable alloy would preserve most of its strength up to approximately 380°C.

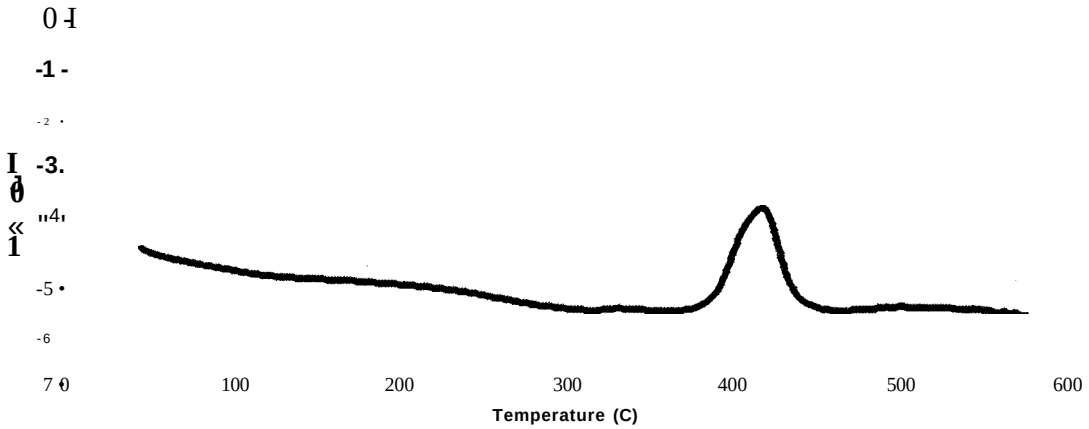

Figure 4.10: DSC plot of the Al-Fe-V-Si atomized powder.

4.2 Al-Fe-V-Si Coatings

The metastable Al-Fe-V-Si coatings were produced using the procedure outlined previously. A first series of coatings were prepared using helium as both the propellant and feeding gas. Coating thicknesses of over 250 jxm in a single pass were achieved, as illustrated in the SEM image shown in figure 4.1 la. It can be observed that the coating is dense, showing porosity level of less than 1%. No visible cracks are present within the coating, or at the coating-substrate interface, which suggests a good bond at the interface. It is accepted that the bonding at the coating-substrate interface and cohesion of the particles within the coating is a result of extensive plastic deformation and the formation

of adiabatic shear instabilities at the particle interface [41]. Thus, the quality of the coating and of the coating/substrate interface reveals that the particle impact velocity was sufficient to induce proper particle deformation upon impact with the substrate. An increased porosity level can be observed in the top layer of the coating (on the top right part of figure 4.11a), where partially deformed and non-deformed particles are present. This has also been reported in other CGDS works where it has been established that the upper layer of the coating does not experience the impinging effect of subsequent impacting particles, which increases the deformation of the underlying layer [42]. An SEM image of the coating at a higher magnification is presented in figure 4.11b. Although it is possible to identify individual feedstock powder particles in this figure it can be observed that the original feedstock powder particles have undergone extensive plastic deformation to form a dense coating.

Figure 4.11: SEM images of (a) the Al-Fe- V-Si coating produced using the Cold Spray process and (b) the microstructure of the coating at a higher magnification.

4.2.1 Velocity Measurements

The measured average particle velocity was 706 ± 90 m/s when helium was used as the propellant gas. Since an appreciable coating thickness was achieved, the particle velocity was higher than the critical velocity of the Al-alloy. Figure 4.12 illustrates the particle velocity distribution, where it can be noted that the particle velocity follows a normal distribution. The particle velocity of the Al-Fe-V-Si alloy powder possessed the fastest

particle velocity compared to other aluminum alloys sprayed at the University of Ottawa Cold Spray Laboratory. These high velocities can be attributed to the higher drag factor associated to the very irregular shape of the Al-Fe-V-Si alloy powder.

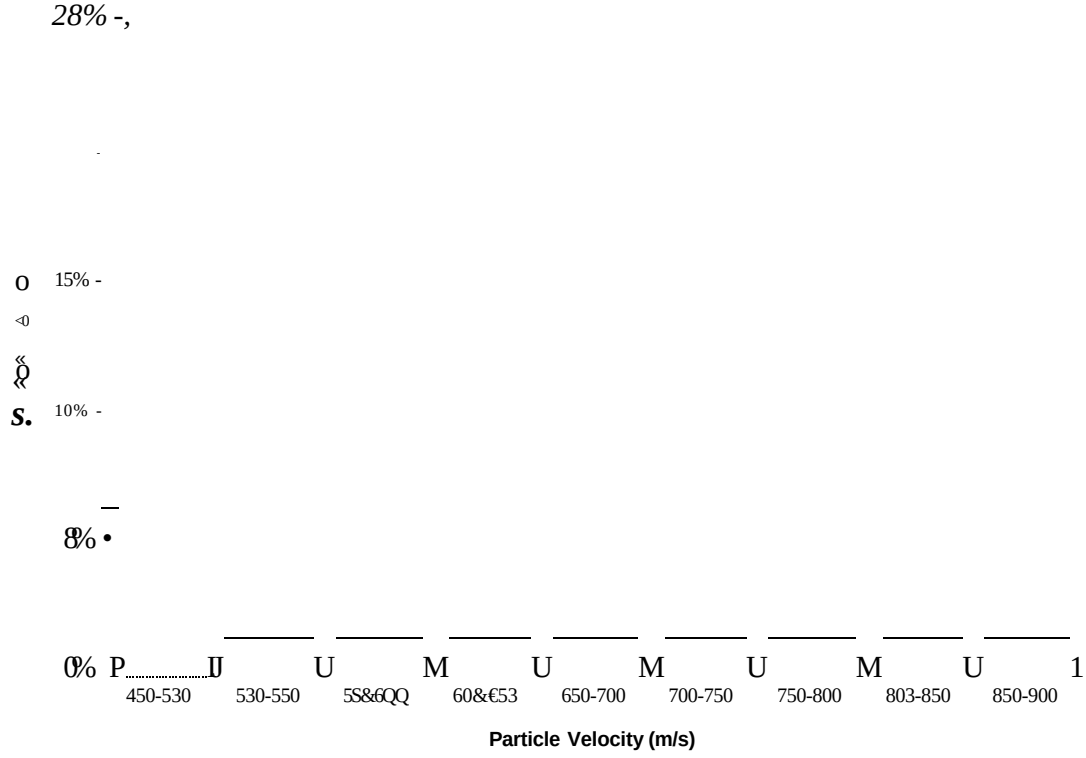

Figure 4.12: Particle velocity distribution of the Al-alloy feedstock powder using helium as the gas supply.

4.2.2 Microstructure and Phase Identification

TEM observations of the microstructure of the Al-Fe-V-Si coatings produced by CGDS reveal the presence of the three zones observed in the original as-atomized feedstock powder. The randomly distributed MI $(Al,Si)_x(Fe,V)$ precipitates can be seen in the Al-matrix of "zone A" as well as in the intergranular areas of the microcellular region "zone

B" of figure 4.13. The same phase can also be observed as the bright regions in the dark field (DF) image shown in figure 4.14, obtained from the ring pattern of the SAED shown in the upper right corner of the same figure.

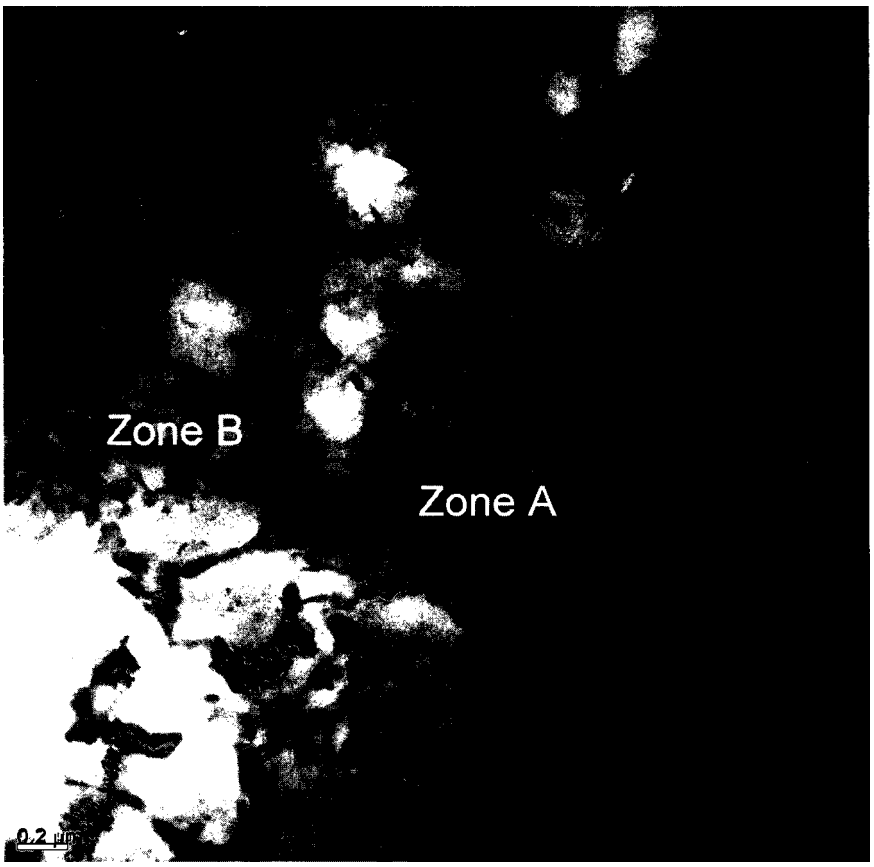

Figure 4.13: Bright-field TEM image illustrating "zone A" and "zone B".

Figure 4.14: Dark-field TEM image showing same area as in figure 4.13.

High-Resolution TEM (HRTEM) observations have also demonstrated the presence of an agglomeration of very fine particles of the MI $(Al,Si)_x(Fe,V)$ phase at the intercellular region in "zone B" as shown in figure 4.13. A bright field (BF) image of the same area is shown at higher magnification in figure 4.15a. The HRTEM image shown in figure 4.15b - corresponding to the highlighted region in figure 4.15a - illustrates the crystalline nature of the A1 matrix having long range periodicity, whereas the very fine MI (QC) phase at the grain interface only demonstrates short range order. Some clusters of atoms are observed, which seem to have some periodicity in the fine MI (QC) phase, but do not have the characteristics of an amorphous phase short-range order.

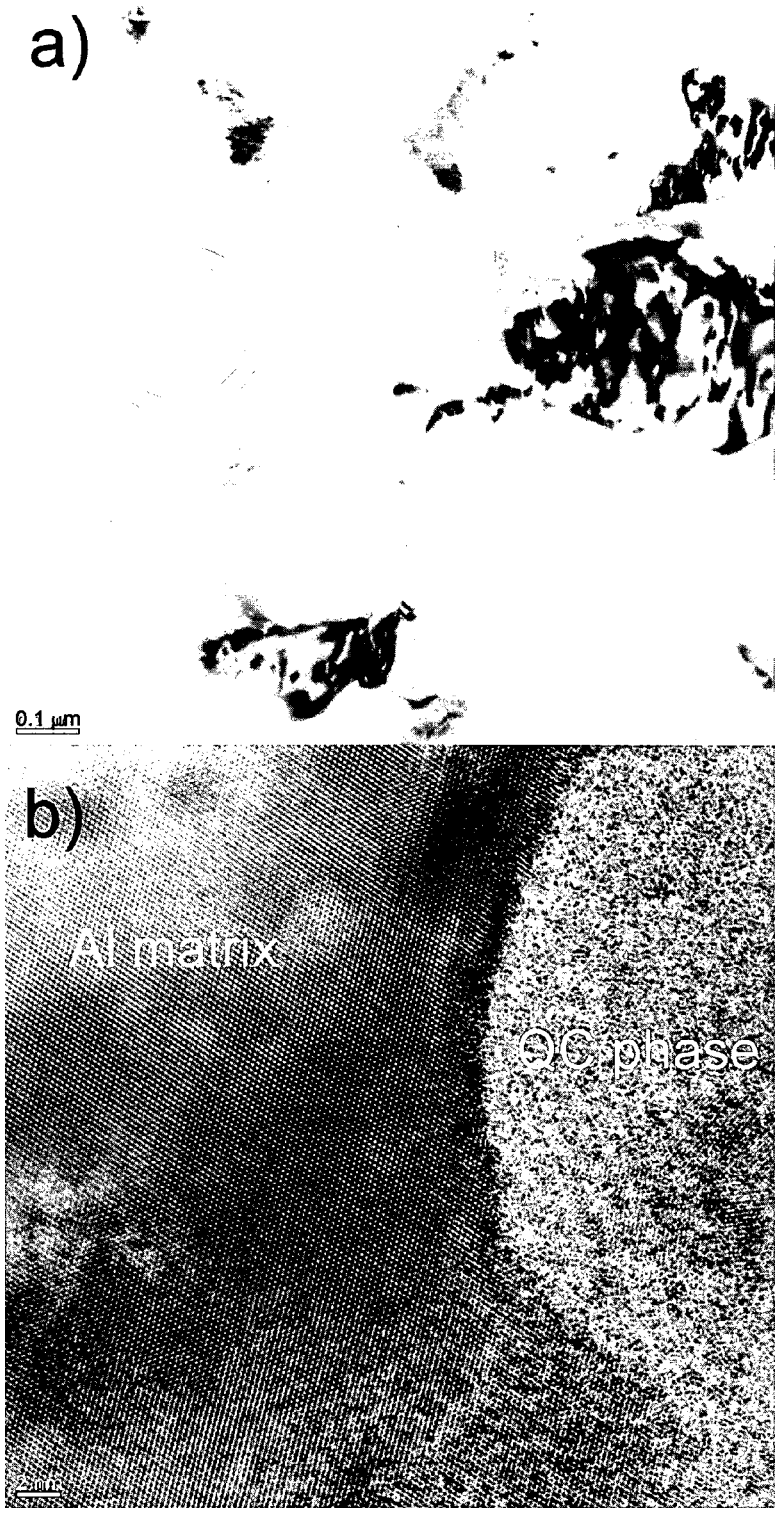

Figure 4.15: Bright-field TEM image of intercellular region of "zone B" (a) and HRTEM image of grain interface (b).

The equiaxed region "Zone C" was also observed in the as-sprayed coating as shown in figure 4.16a. The grains in this region appear coarser and less elongated than in "Zone B" and the intercellular region is composed of the Ali3(Fe,V)3Si silicide phase, as determined by indexing of diffraction pattern. In figure 4.16b, the precipitates within the grains appear to have agglomerated in globular clusters of $(Al,Si)_x(Fe,V)$ MI phase (GCMI). It is believed that the agglomeration of the MI phase is due to the slower growth of the A1 matrix in "zone C" during solidification thus allowing the MI phase to grow further than in "zones" A and B [40].

Since all the microstructural characteristics of the Al-Fe-V-Si alloy found in the feedstock powder are also found in the CGDS coatings, it can be concluded that the microstructure of the Al-Fe-V-Si alloy is unaffected by the CGDS process following these TEM observations.

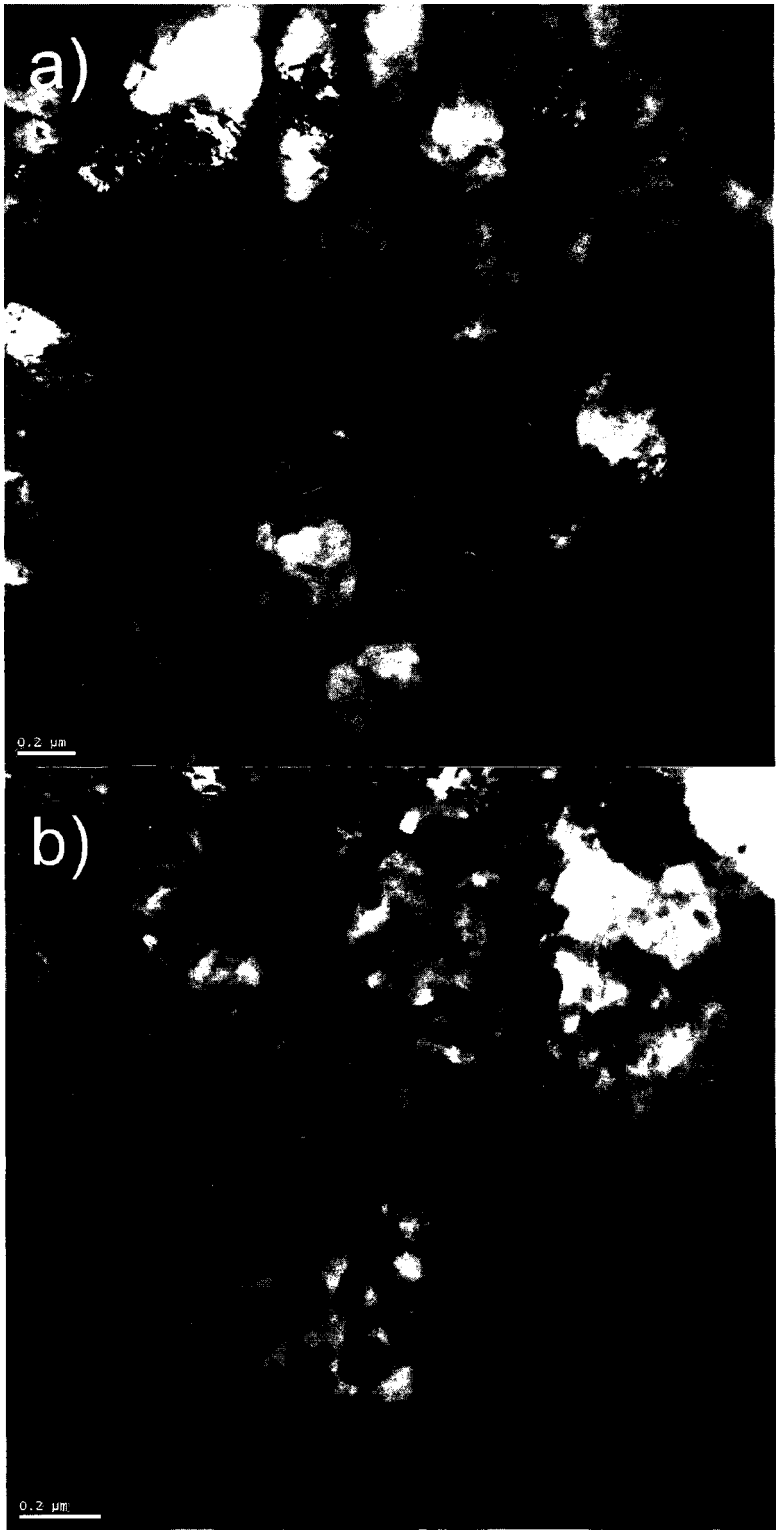

Figure 4.16: Bright-field TEM image of "zone C" (a), and higher magnification image demonstrating the GCMIphase (b).

4.2.3 Aging

4.2.3.1 Controlled Aging

The TEM observation of the aged Al-alloy coatings reveals that the homogeneously dispersed precipitates in Al-matrix and microcellular regions, respectively "zone A" and "zone B", are still present and were not significantly affected by the heat treatment at 400°C. for 96 hrs. In the center of figure 4.17, "zone A" appears identical to the observations made of the feedstock powder and the as-sprayed coating. However, there appears to be some coarsening of the dispersed precipitates in "zone A".

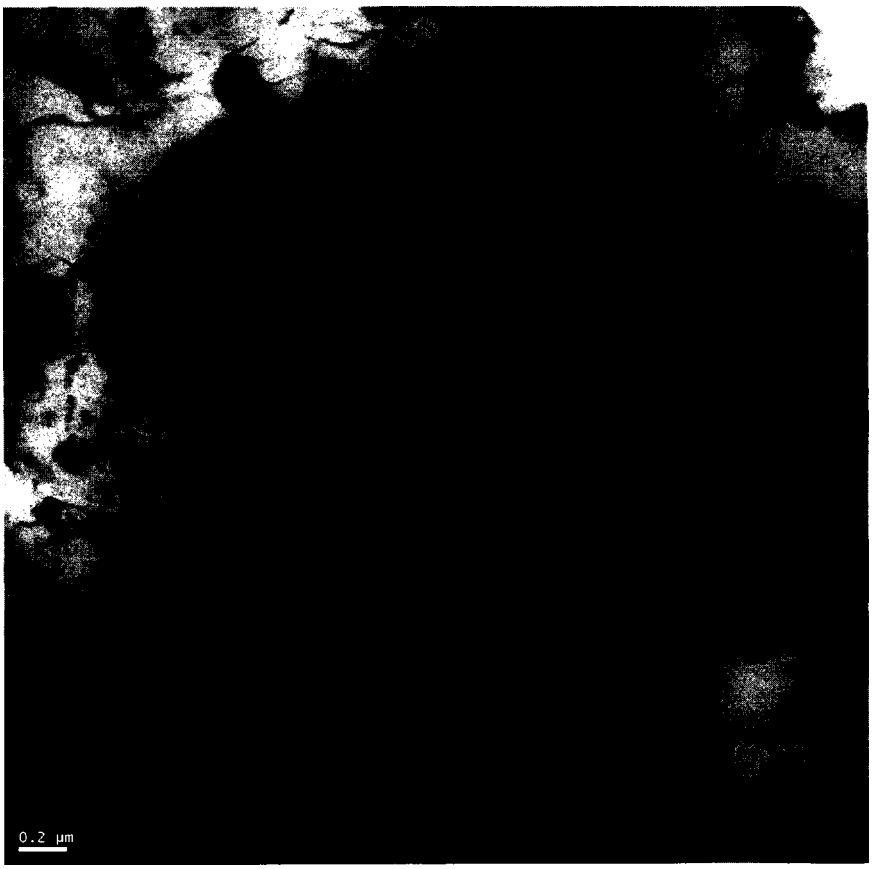

Figure 4.17: Bright-field TEM image of precipitates in "zone A".

It is noted that the intercellular sections of the equiaxed region "zone C" appears to be broken down as a result of the aging. The intercellular sections, which were intact prior to aging, are now sectioned into smaller elongated particles as shown in figure 4.18. Furthermore, the intercellular sections in "zone C" also appear to have undergone some crystallization as diffraction contrast can now be observed within the grain interface, which was not present before aging. When the grain interface (figure 4.19) is observed under HRTEM, it can be seen that the phase in this region is now crystalline in nature (left side of figure 4.19) due to the long-range periodicity similar to that of the Al-matrix (right of figure 4.19).

Figure 4.18: Bright-field TEM image of "zone C" in aged sample.

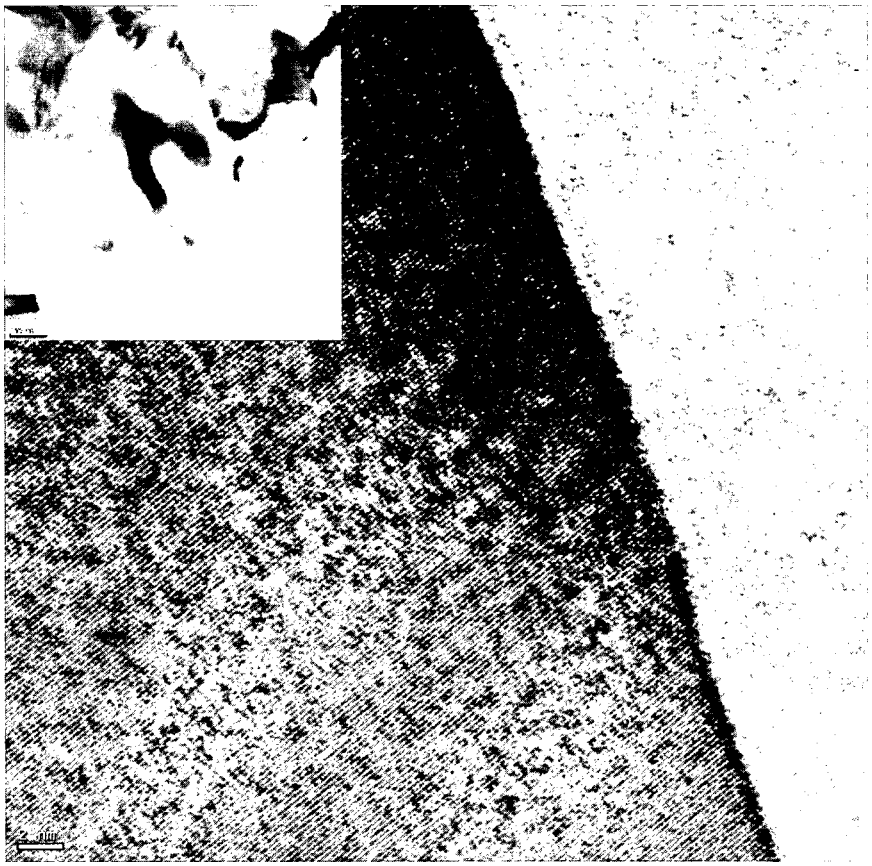

Figure 4.19: HRTEM image showing crystalline nature of intercellular phase.

The particles formed from cluster of MI (QC) within the equiaxed region "zone C" also appear coarser after aging as shown in figure 4.20. The diffraction pattern of a single MI (QC) particle (figure 4.21) demonstrates crystallograhically forbidden symmetries, meaning they are forbidden for periodic crystals and cannot be formed in 3-D space by modifying an underlying periodic structure possessing the same symmetry.

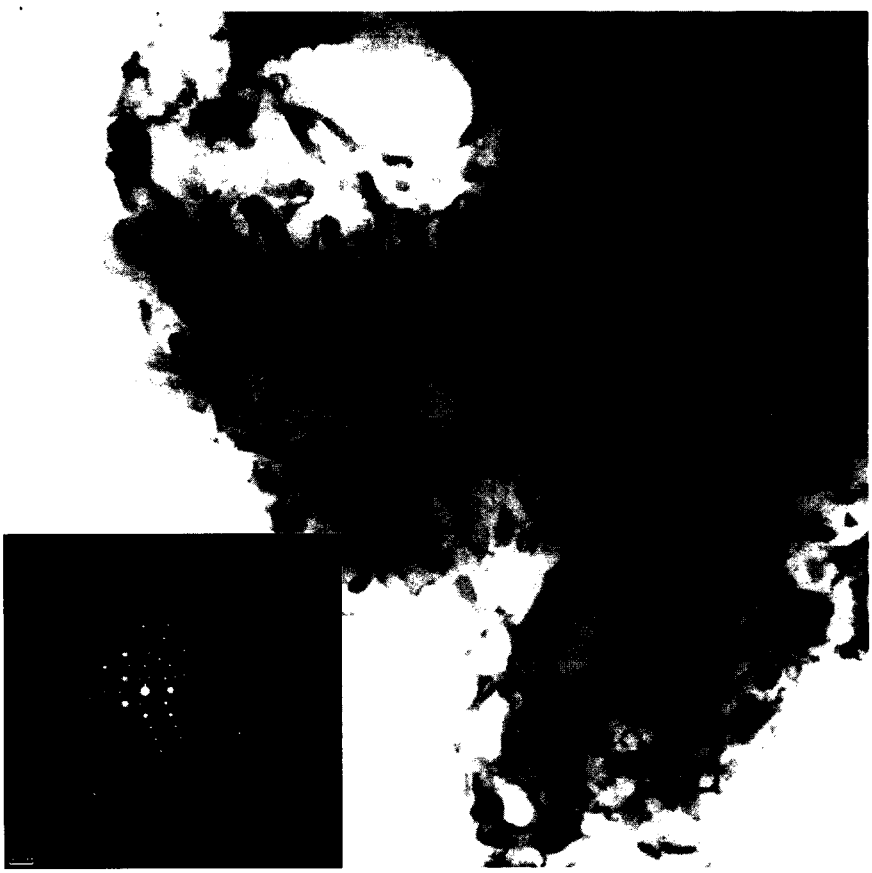

Figure 4.20: Bright-field TEM image of CGMI phase.

Figure 4.21: Bright-field TEM image of one single QC showing crystallographically forbidden reflections.

4.2.3.2 In-situ Accelerated Aging

A piston coated with the Al-Fe-V-Si alloy using the cold process was installed in a test engine. After 300 hours of operation, the piston was removed and inspected. Results showed that the coating remained intact, and that no peeling had occurred. Therefore, it is extrapolated that the bond strength of the Al-Fe-V-Si coating is sufficiently high to prevent failure in an IC engine.

4.2.4 Microharness

The average microhardness of the as-sprayed Al-alloy coatings, using helium as the propellant gas, was found to be $_{HV300}$ = 172 ± 3. The microhardness values obtained in the top layer of the coating were significantly lower than that of the coating. Due to the nature of the CGDS process, the uppermost layer of the coating does not undergo as much impingement of particles as the lower portion. Therefore, the top layer of the coating is more porous (less dense) than the underlying layer and as such would demonstrate lower microhardness values. A subsequent machining process can remove the higher porosity portion of the coating.

The coating samples aged at 400°C for 96 hours exhibited an average microhardness of $_{HV300}$ = 114 ± 3. This represents a reduction in microhardness of 37%, most likely due to the microstructural changes observed in "zone C" with TEM. The energy input during aging appears to initiate minimal coarsening of the microstructure, resulting in a slight increase in ductility and toughness at the expense of microhardness. By comparison, the substrate suffered a loss of 67% in microhardness under the same conditions.

Similarly, microhardness was evaluated at two different locations on the piston coating, after accelerated aging, to get a better average due to the temperature gradient present on the piston crown. The values obtained are $_{HV300}$ = 114 ± 9 and $_{HV300}$ = 135 ± 4. The microhardness values are equal or higher than those obtained from controlled aging at 400°C for 96 hours. This indicates that the Al-alloy does preserve its high mechanical properties in an actual IC engine. By comparison, microhardness measured near the

surface of uncoated sections of the piston demonstrated average values of $_{HV300}$ = 99 ± 1, which shows that current alloy systems used in piston manufacturing possess inferior mechanical properties than the proposed Al-Fe-V-Si alloy when exposed to such high-temperature environments.

4.3 Nitrogen Process and Composite Coatings

A second series of coatings were produced using nitrogen as the propellant and feeding gas. However, it was noted that dense qoatings could not be achieved using the pure Al-Fe-V-Si feedstock powder and nitrogen. To overcome this, a composite feedstock powder was created by mechanically mixing 25% vol. alumina particles with the Al-alloy powder prior to spraying. The alumina particles have a non-spherical morphology and are approximately 10 to 20 (j.m in diameter. By adding hard particles (i.e. alumina) to the original feedstock powder, it is envisioned that the impingement effect is increased by the impact of the alumina particles onto the partially deformed feedstock particles within the coating. In the process, it is expected that some of the alumina particles become entrapped in the coating. Thus, despite lower Al-alloy powder particle velocities, it is expected that dense coatings could be formed.

4.3.1 General Microstructure

A coating thickness of approximately 250 |xm was achieved in a single pass using the composite powder and nitrogen as the propellant and feeding gas. The alumina particles appear lighter on the SEM image of the composite coating shown in figure 4.22. The

coating is dense throughout (less than 1% porosity) with the exception of the top layer as observed in the coatings produced with the pure Al-alloy powder and helium. There are no cracks within the coating or at the coating-substrate interface. A higher magnification SEM image (Fig. 4.23) demonstrates that the alumina particles do not affect the complex microstructure of the Al-alloy, which is still preserved during the spraying process. Some porosity can be observed around the perimeter of the alumina particles (dark grey). The presence of the porosity is the result the softer A1 alloy particles that do not completely deform around the hard alumina particles. Moreover, hard alumina particles cannot plastically deform on contact with the A1 alloy particles, hence preventing the formation of a dense bonding surface between alumina and A1 alloy powder particles. Approximately 14% vol. alumina particles are present in the coating, compared to the original 25% vol. in the composite feedstock powder, which represents a loss of 44% vol. Similar results, showing a decreased concentration of alumina particles retained within the coating, when using up to 70% vol. alumina, have been reported in the literature [43]. It is expected that the presence of alumina should not significantly affect the performance of the coating. The sharp edges of the hard alumina particles may act as stress concentrations within the coating, thus possibly decreasing its fatigue resistance. A crack may initiate at the end of a sharp edge and propagate through the coating until failure. A coating failure inside an IC engine during operation could potentially cause serious damage to other internal parts. Alternatively, the insulation properties of alumina, due to its low thermal conductivity compared to aluminum, may reduce the overall thermal conductivity of the coating, thus further improving fuel efficiency of the coated engine.

The less heat conducted through the piston, the more heat (available energy) can be used during the power stroke of engine cycle, thus increasing the engine output for a given fuel input.

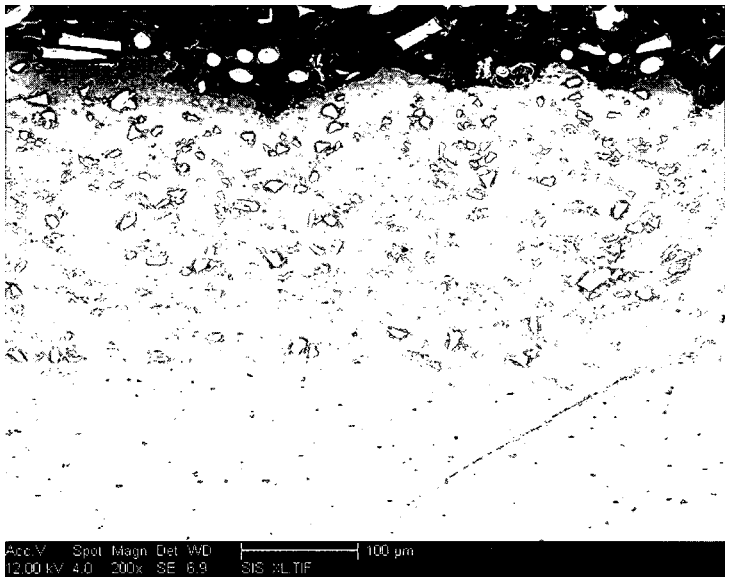

Figure 4.22: SEM images of the coating resulting from the composite powder.

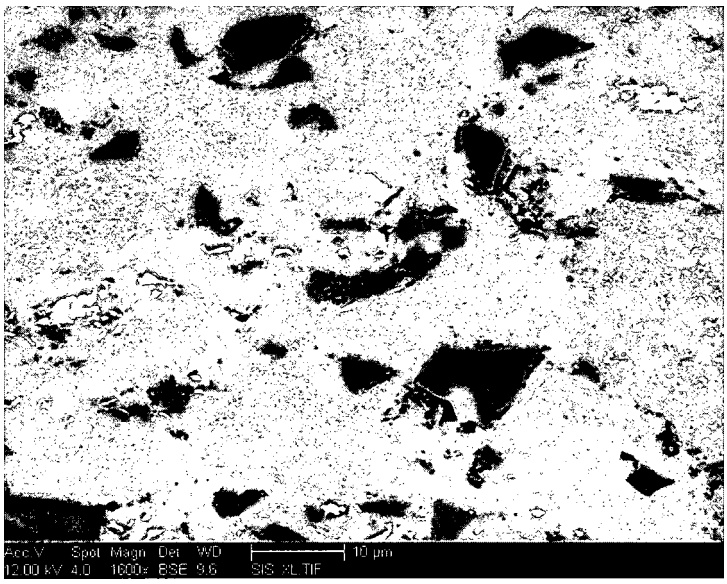

Figure 4.23: Higher magnification SEM image of the microstructure of the composite coating.

4.3.2 Velocity Measurements

When using pure Al-Fe-V-Si feedstock powder and nitrogen as the gas supply, an average particle velocity of 420 ± 74 m/s was recorded. As was noted previously, deposition did not occur using these spraying parameters, and thus would indicate that the particle velocity is below the critical velocity of the alloy. However, when adding alumina particles to the feedstock powder, successful deposition is achieved with an average measured particle velocity of 419 ± 72 m/s, which is almost identical to the velocity of the pure feedstock powder. It is suggested that the pure Al-alloy particles do not undergo enough plastic deformation at this velocity to produce a coating, but the addition of the hard alumina particles increases the plastic deformation of the Al-alloy particles significantly by means of impingement of the underlying layers in order to produce a coating without affecting the average particle velocity. All the kinetic energy of the alumina particles is transferred to plastic deformation of the underlying Al-alloy particles. Figure 4.24 shows the particle velocity distribution of the pure feedstock powder, and composite power using nitrogen as the gas supply. Both cases follow a normal velocity distribution with a single peak, and it can be concluded from these measurements that the addition of alumina particles in the feedstock powder does not affect the particle velocity.

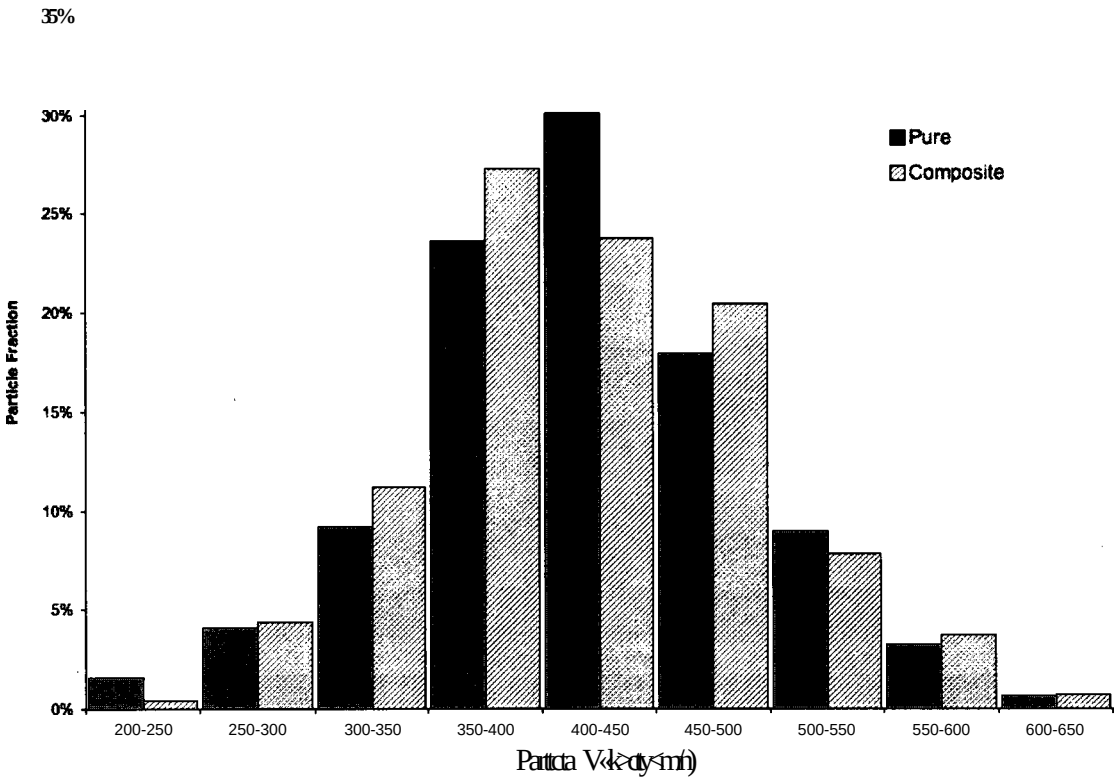

Figure 4.24: Particle velocity distribution using nitrogen with comparison between pure feedstock powder and Al-alloy/Alumina composite powder.

4.3.3 Adhesion Strength

The coating-substrate interface bonding quality and inter-particle cohesion strength level was assessed using the ASTM standard described previously. Coating failure occurs if all of the coating detaches from the substrate and remains bonded to the adhesive, while adhesive failure occurs if all the coating remains bonded to the sample. Cohesive failure occurs when the failure is located within the coating, meaning that the bottom of the coating remains attached to the substrate and the top of the coating remains bonded to the

adhesive. Finally, mixed-mode failure is a combination of the above, which means that some of the coating may remain attached to the substrate while other sections of the coating may have debonded.

The average bond strength of the samples sprayed using nitrogen was 44.5 ±1.8 MPa. The failure mode was determined to be cohesive according to the standard, meaning the failure occurred within the coating itself. As seen in figure 4.25, both surfaces (substrate and adhesive) are covered with the coating, indicating that the failure was contained in the coating. These results confirm a good adhesion at the coating-substrate interface, as was predicted by the SEM images of the coatings. Similar coating systems, namely the metallic bond coat of a thermal barrier coating for diesel engine pistons have reported lower bond strength values. The bond strength of bond coats produced by HYOF possessed an average of 33.3 MPa [44]. Another study showed that bond coats produced by plasma spraying using a 100% metallic feedstock powder had average bond strength of 29 MPa A composite mixture of 50% wt metallic with 50% wt ceramic feedstock powder resulted in a reduced average bond strength of the coating to 15 MPa [45]. The average bond strength of the composite powder used in this study is three times higher than the average value obtained using a similar composite mix using a conventional spraying technique (i.e. plasma spray). Therefore, it is assumed that the CGDS composite coating would not detach under normal operating conditions since its bond strength is superior to current values of other coating technologies.

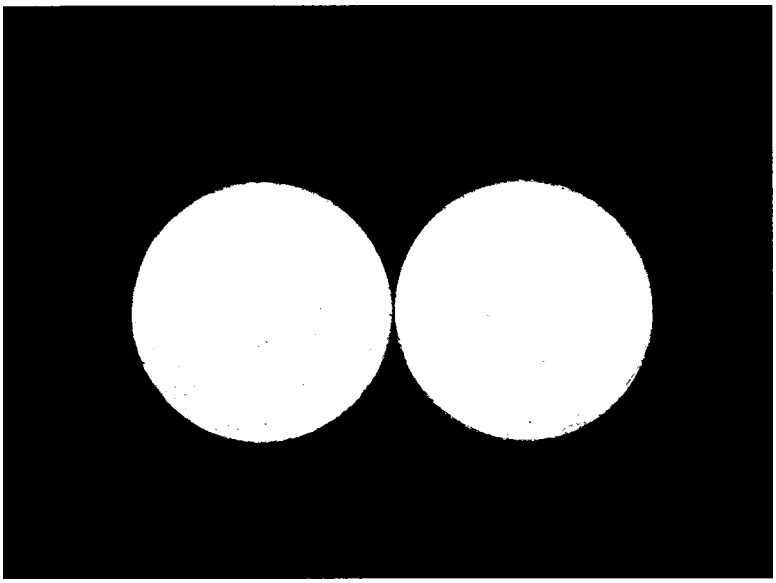

Figure 4.25: Cohesive failure of bond specimen.

4.4 TEM Observations of Bonding Interface

The bonding mechanism responsible for the formation of uniform and dense coatings during the CGDS process is still not quite well understood. Most researchers in this field tend to agree that the bonding between powder particles within the coating is due to adiabatic shear instabilities, which are created at the outer surface of the powder particle at the moment of impact. Although the theory could not be proven during this study, some interesting TEM observations may help in giving more insight on general microstructural characteristics of a powder particle-particle interface in a CGDS coating, based on the observations of CGDS coatings of Al-Fe-V-Si alloy powder. The following observation were obtained from the same coating samples as in section 4.2, Al-Fe-V-Si alloy powder, using helium as the propellant and feeding gas.

A region of high deformation is observed in the powder particle seen in the upper portion of figure 4.26, where diffraction contrast is only seen in certain section of a single grain. The diffraction contrast is due to the presence of sub-grains, which are created when a material is subjected to intense deformation. The area of high deformation shown in figure 4.26 is most likely a particle-particle interface site between two different powder particles. At higher magnification, a sharp demarcation between different microstructures is seen in the upper section of figure 4.27. The region of high-deformation, where sub-grains are present, is very thin and only present in what is suspected to be the outer particle boundary. The area that extends from this high-deformation region towards the center of the powder particle possesses an undisturbed microstructure, or general microstructure as described thus far. Therefore, the boding mechanism responsible for coating formation in CGDS appears to be very localized at the outer edge of the powder particle. The affected area at the powder particle boundary is quite thin, as it does not go very deep into the particle core. Rather, the particle core only appears to undergo only pure plastic deformation.

Figure 4.26: Bright-field TEM image of sub-grains at particle-particle interface.

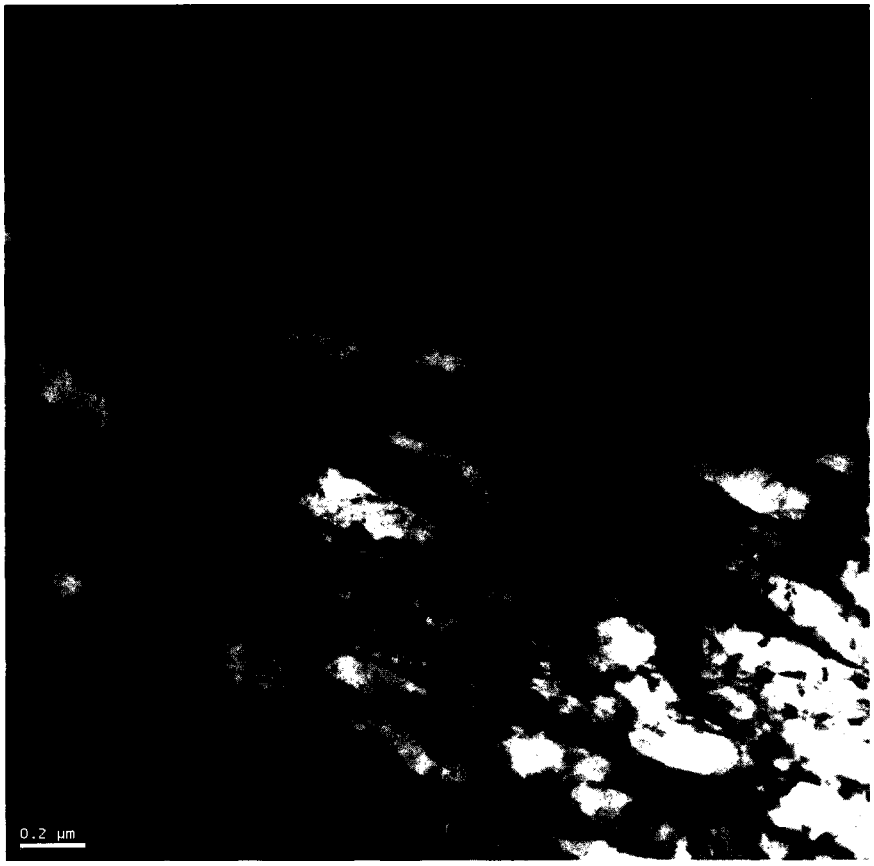

Figure 4.27: Higher magnification bright-field TEM image, showing localized changes in microstrucutre at particle-particle interface.

5 Conclusions

The objectives of this research were to manufacture a high-temperature resistant Al-alloy, for internal combustion engines, by means of rapid solidification and subsequently produce coatings using the Cold Gas Dynamic Spraying process. Furthermore, the feasibility of using this technology to produce coatings in a large-scale industrial process was also investigated using nitrogen as the process gas instead of helium gas. Outlined in this chapter are the major milestones of this study as well as recommendations and suggestions should this study be continued by others.

5.1 Powder Production

The gas atomization process successfully produced the Al-Fe-V-Si alloy powder from master alloys, with a process yield of 55 %wt per batch. However, re-using rejected powder particles in the melt of the subsequent batch could increase the overall process yield. The particular composition of the Al-Fe-V-Si alloy made it somewhat difficult to smoothly atomize due to its high viscosity, however increasing the atomizing pressure to 9.4 MPa and temperature to 840°C remedied the situation.

The resulting powder particles are spherical and range in size from 5 p.m to 60 jam in diameter. Smaller particles agglomerate to larger particles, which result in irregular particle morphology. The irregular-shaped powder particles have a higher drag

coefficient, creating higher velocities during the CGDS process, which ultimately means denser coatings. This was validated by in-flight particle velocity measurements and the low-porosity of the coating.

Electronic microscopy investigations revealed that the atomized Al-Fe-V-Si alloy powder particles contain three different internal microstructures, named "zones" A, B and C. "Zone A" is composed of fine homogeneously distributed intermetallic precipitates in a a-Al matrix, "zone B" is composed of microcellular elongated grains with precipitates found at the intergranular region, and finally "zone C" is made of coarser, equiaxed grains, with precipitates in both the a-Al matrix and the intergranular region. The microstructure was also found to be dependant on particle diameter. Small powder particles, such as agglomerated satellites of approximately 1 jam or less, only possess "zone A" and "zone B" microstructures, while larger particles, larger than 5 fj.m, are generally composed of all three zones.

Furthermore, two phases which compose the intermetallic precipitates were identified; a $(Al,Si)_x(Fe,V)$ micro-quasicrystalline icosahedral (MI) phase and a bcc Ali3(Fe,V)3Si silicide phase. The MI phase is found in all three "zones", while the silicide phase only appears in "zone C". The thermal stability of the MI phase was established by DSC analysis to be stable up to 380°C.

5.2 Coatings Produced by CGDS

Coatings made of the Al-alloy powder were sprayed at the University of Ottawa Cold Spray Laboratory, using helium and nitrogen as process gases. The stagnation pressure and temperature were 1 MPa and 250°C respectively for each trial. Using helium as the propellant gas, an average particle velocity of 706 m/s was achieved, which resulted in dense coatings having less than 1% porosity, and a thickness of 250 |4,m in a single pass. The same microstructural characteristics and intermetallic phases were found within the coating, demonstrating that the Al-alloy is unaffected by the CGDS process.

Aging performed in a temperature-controlled furnace at 400°C showed that the Al-Fe-V-Si alloy remained unchanged. "Zones" A and B were similar to those in the powder particles. Only a small change was noticed in "zone C", where the intercellular region appears to have undergone some crystallization. Furthermore, the MI phase particles within the a-Al matrix have demonstrated a limited amount of coarsening.

Microhardness testing also demonstrated that exposing the Al-alloy to a temperature of 400°C has some effect on the strength of the coating, however less important than conventional alloys. Prior to aging, the coating achieved an average hardness value of 172 $_{HV300.}$ The microhardness of the aged coating dropped 37% to an average value of 114 **HV**3OO- By comparison, the substrates suffered a loss of 67% under the same conditions.

A sample sprayed onto an IC engine piston, which was run in a test engine, showed that the coating remained intact and did not peel or delaminate.

When using nitrogen as the process gas, coatings could not be formed using the Al-Fe-V-Si powder only. A composite powder mixture was created from the Al-alloy and alumina particles. With the composite powder, coatings of 250 jim in thickness where achieved. A mixture ratio of 3:1 by volume was used, which resulted in 14% vol. of alumina particles entrapped in the coating. In flight velocity measurements showed an average particle velocities of 420 m/s. The velocity is lower than critical velocity for aluminum, which is why coating formation did not occur when using the Al-alloy powder alone. However, the addition of the alumina particles to the feedstock powder did not affect average particle velocity. Therefore another mechanism is responsible for the coating formation, and was deemed to be the impingement effect of the hard alumina particles onto the more ductile alloy particles, which made then deform and adhere to the substrate and each other.

Investigation by electronic microscopy revealed that the microstructure of the Al-Fe-V-Si is not modified in the coating by the addition of alumina particles. It is also thought that the alumina particles could be beneficial to the coating performance as they may reduce the thermal conductivity of the coating, further protecting the substrate. The downside is that the sharp edges of the alumina particles inside the coating may act as stress concentrations, but coating adhesion testing demonstrated that the average bond value of 44.5 MPa was more than adequate, when compared to similar applications.

5.3 Final Word and Recommendations

Although it was demonstrated that an Al-Fe-V-Si alloy, resistant to temperatures up to 380°C, can be produced by gas atomization and that the CGDS process was successful in producing coatings of this alloy without affect its microstructure nor its thermal stability, there still remains further investigation to show the potential of this alloy for the automobile industry.

The study can be completed in various steps simultaneously, or a different times. Here are outlined the major guidelines as to what steps remain to have a comprehensive study. Primarily, the composition of the alloy should be optimized by varying the concentration of the alloying elements in order to get the best possible combination of physical properties and thermal stability. An aging curve should also be determined for each specific alloy composition to show the thermal stability of the alloy at a given temperature as a function of time. The atomization process can also be revised to increase the process yield, and also investigate the advantages of re-melting the large powder particles not useable for the CGDS process in a subsequent atomization batch.

Efforts pertaining to the CGDS process should be concentrated on using nitrogen as the process gas, as it is better suited for large-scale manufacturing for economical reasons. This also means that composite powder mix proportions should be optimized to obtain the best coating properties. It would also be possible to experiment with other hard material powders, other than alumina.

Further investigation should also be done on the effects of adding hard particles, such as alumina, into the coating. For example, what are the consequences on thermal conductivity of the coating, the effects on the resistance of the coating to peeling or delamination, erosion, or corrosion due to combustion gases?

Once it has been established that the coating process is optimized for commercial coating production, engine performance testing should be evaluated. An IC engine baseline performance should be determined using an engine and dynamometer. The pistons would then be coated using the Al-Fe-V-Si alloy and its performance compared to the baseline. Ideally, the engine would be tested under various load conditions to represent an average daily driven automobile. At this point, it would also be a good opportunity to test for gas emissions difference between the uncoated and coated engine, to show if there is a significant increase in nitrous oxides emissions. Eventually, a coated engine could be installed in a car and have its real world performance evaluated and compared to the same model, but with an uncoated engine. Ultimately, entire parts could be fabricated of the metastable Al-Fe-V-Si alloy using the CGDS process.

References

1. Thorpe, S. G., Fuel Economy Standards, New Vehicle Sales, and Average Fuel Efficiency, *J. Regul. Econ., 2007,* Vol. 11, p. 311-326
2. National Commission on Energy Policy: 2004, Ending the Energy Stalemate: A Bipartisan Strategy to Meet America's Energy Needs, Washington, DC, July 2006
3. Romm, J., Energy and American Society - Thirteen Myths, Springer, 2007, p. 103-124
4. Energy Information Administration: 2006, Annual Energy Outlook 2006, DOE/EIA-0383 (2006), Washington, DC
5. International Energy Agency: 2004, Biofuels for Transport Press Release, International Energy Agency, Paris
6. Romm, J., The Car and the Fuel of the Future: A Technology and Policy Overview, National Commission on Energy Policy, Washington, DC, 2004
7. I. Taymaz, K. £akir, A. Mimaroglu, Experiment study of effective efficiency in a ceramic coated diesel engine, *Surf. Coat. Technol.,* Vol 200 (2005) 1182-1185
8. C. R. Ferguson, A.T. Kirkpatrick, *Interna! Combustion Engines,* Second Edition, John Wiley and Sons, 2001
9. E. Buyukkaya, T. Engin, M. Cerit, Effect of thermal barrier coating on gas emissions and performance of a LHR engine with different injection timings and valve adjustments, *Energ. Corners. Manage.,* Vol 47 (2006) 1298-1310
10.1. Taymaz, K. £akir, A. Mimaroglu, Experiment study of effective efficiency in a ceramic coated diesel engine, *Surf Coat. Techno!.,* Vol 200 (2005) 1182-1185

11. N.A. Belov, A.A. Aksenov and D.G. Eskin, Iron in Aluminum Alloys: Impurity and Alloying Element, Ed. Taylor and Francis, London, 2002, Chapter 4
12. E. Buyukkaya, Thermal analysis of functionally graded coating AISi and steel pistons, *Surf. Coat. Technol.,* 2008
13. Dobatkin, V.I. Yelagin, V.I. and Fedorov V.M., Bystrozakristalliozovannye alyuminievye splavy, Moscow, VILS , 1995
14. C. M. Adam, V. R. V. Ramanan and D. J. Skinner, in E. W. Collings and C. C. Koch (eds.), *Under cooled Alloy Phases,* The Metallurgical Society, Warrendale, PA, 1987, p. 59
15. D.J. Skinner, V.R.V. Ramanan, M.S. Zedalis and N.J. Kim, Stability of Quasicrystalline Phases in AI-Fe-V Alloys, *Materials Science and Engineering, 99 (1988)* 407-411
16. W. J. Park, S. Ahn and Nack J. Kim, Evolution of microstructure in a rapidly solidified Al-Fe-V-Si alloy, *Materials Science and Engineering, A189* (1994) 291-299
17. B. Mais and R. Ruthardt, *Powder Metallurgy Data,* Volume 2A1, Springer Berlin Heidelberg, Chapter 2
18. P. Fauchais, A. Vardelle, and B. Dussoubs, *Quo Vadis Thermal Spraying?,* J. Therm. Spray Technol, Vol. 10 (2001) 44-66
19. B. Jodoin, P. Richer, G, Berube, L. Ajdelsztajn, A. Erdi-Betchi, M. Yandouzi, Pulsed-Gas Dynamic Spraying: Process analysis, development and selected coating examples, *Surf. Coat. Technol 201* (2007) 7544-7551

20. L. Ajdelsztajn, B. Jodoin, G.E. Kim, J. Schoenung and J. Mondoux, Cold Spray Deposition of Nanocrystalline Aluminum Alloys, *Meta.ll. Mater. Trans. A,* Vol 36, 2005, p.657-666

21. T. Stoltenhoff, H. Kreye and H.J. Richter, An Analysis of the Cold Spray Process and its Coatings, *J. Therm. Spray Technol.,* Vol 11 (No. 4), 2002, p. 542-550

22. H. Assadi, F. Gartner, T. Stoltenhoff, and H. Kreye, Bonding mechanism in cold gas spraying, *Acta Mater,* Vol 51, 2003, p. 4379-4394

23. L. Ajdelsztajn, A. Zuniga, B. Jodoin and E. Lavern, Cold Gas Dynamic Spraying of a High Temperature A1 Alloy, *Surf. Coat. Technol.,* Vol 201 (No. 6) 2109-2116

24. B. Jodoin, Mach Number Limitation in Cold Spray, *J. Therm. Spray Technol.,* Vol 11 (No 4), 2002, p. 496-507

25. T. Van Steenkiste, J.R. Smith, Evaluation of Coating Produced via Kinetic and Cold Spray Processes. *J. Therm. Spray Technol.* Vol. 13 (2) (2004) 274-282

26. R.C. Dykhyizen, M.F. Smith, Gas Dynamic Principles of Cold Spray. *J. Therm. Spray Technol.* Vol. 7 (2) (1998) 205-212

27. M. Grujicic, J.R. Saylor, D.E. Beasley, W.S. DeRosset, D. Helfritch, Computational Analysis of the Interfacial Between Feed-powder Particles and the Substrate in the Cold-gas Dynamic-spray Process, *Applied Surface Science* 219 (2003) 211-227

28. A.P. Alkhimov, A.N. Papyrin, V.F. Kosarev, N.I. Nesterovich and M.M. Shushpanov, Gas Dynamic Spray Method for Applying a Coating, U.S. Patent 5, 302,414 April 12 1994

29. A.H. Shapiro, The Dynamics and Thermodynamics of Compressible Fluid Flow, The Ronald Press Company, New York. 1953

30. D.L. Gilmore, R.C. Dykhuizen, R.A. Neiser, T.J. Roemer, and M.F. Smith, Particle velocity and Deposition Efficiency in the Cold Spray Process, *J. Therm. Spray Technol.,* Vol 8 (4), 576-582

31. B. Jodoin, F. Raletz and M. Vardelle, Cold Spray Modelling and Validation Using and optical Diagnostic Method. *Surf. Coat. Technol.* 2006, 200 (14-15) 4424-4432

32. K. Taylor, Development of Functionally Graded Titanium and Hydroxyapatite Coatings for Bone Implantation with the use of a Cold Gas Dynamic Spraying System, *M.Sc.A. thesis,* Department of Mechanical Engineering, University of Ottawa, 2006

33. E. Sansoucy, Development of Conventional and Nanocrystalline-Based Coatings Produced by Cold Gas Dynamic Spraying, *Ph. D. thesis,* Department of Mechanical Engineering, University of Ottawa, 2008

34. L. Ajdelsztajn, A. Zuniga, B. Jodoin and E. Lavern, Cold Gas Dynamic Spraying of a High Temperature A1 Alloy, *Surf. Coat. Technol.,* in press

35. R. G. Maev, V. Leshchynsky, Air Gas Dynamic Spraying of Powder Mixtures: Theory and Application, *J. Therm. Spray Technol.,* Vol. 15 (No 2), 2006, p. 198-205

36. "Standard Test Method for Adhesion or Cohesion Strength of Thermal Spray Coatings," C 633-01, *Annual Book of ASTM Standards,* Vol 02.05, ASTM

37. C.J. Li, W.Y. Li, H. Liao, Examination of the Critical Velocity for Deposition of Particles in Cold Spraying, *J. Therm. Spray Technol.,* Vol. 15 (No 2), 2006, p. 212-**222**

38. DPV-2000 - Reference Manual Rev. 5.0, Tecnar Automation, 45 pages

39. L. Ajdelsztajn, A. Zuniga, B. Jodoin, E.J. Lavernia, Cold Spray Processing of a Nanocrystalline Al-Cu-Mg-Fe-Ni Alloy with Sc, *J. Therm. Spray Technol.* Vol 15 (No 2), 2006, p. 184-190

40. R. Tongsri, E.J. Minay, R.P. Thackray, R.J. Dashwood, H.B. McShane, Microstructure and their stability in rapidly solidified Al-Fe-(V,Si) alloy powders, *Journal of Materials Science,* Vol 36, 2000, p. 1845-1856

41. A. N. Papyrin, V. F. Kosarev, S. V. Klinkov, A. P. Alkhimov, Proc. International Thermal Spray Conference, 2002, pp. 380-84

42. T.H. Van Steenkiste, J.R. Smith and R.E. Teetse, Aluminum Coatings via Kinetic Spray with Relatively Large Powder Particles, *Surf. Coat. Technol.,* Vol 154 (No. 2-3), 2002, p. 237-252

43. E. Irissou, J-G. Legoux, B. Arsenault, C. Moreau, Investigation of AI-AI2O3 Cold Spray Coating Formation and Properties, *J. Therm. Spray Technol.,* Vol. 16, 2007, p. **661-668**

44. C. R. C. Lima, J. M. Guilemany, Adhesion Improvements of Thermal Barrier Coatings with HVOF thermally sprayed bond coats, *Surf. Coat. Techol.,* Vol 201, 2007, p. 4694-4701

45. C. R. C. Lima, R. de E. Trevisan, Temperature Measurements and Adhesion Properties of Plasma Sprayed Thermal Barrier Coatings, *J. Therm. Spray Technol.,* Vol. 8 (No 2), 1999, p. 323-327